Monthly Notices of the ROYAL ASTRONOMICAL SOCIETY

MNRAS **549,** 1–20 (2026)
Advance Access publication 2026 April 15

https://doi.org/10.1093/mnras/stag710

Hidden Gems in *TESS*: SHERLOCK finds two new rocky planets around nearby M dwarfs

M. Timmermans,[1,2★] M. Dévora-Pajares,[3,4] F. J. Pozuelos,[5] K. Barkaoui,[6,2,7] B. Rojas-Ayala,[8] J. M. Almenara,[9,10] S. B. Howell,[11] A. H. M. J. Triaud,[1] M. Gillon,[2] M. G. Scott,[1] Y. T. Davis,[1] B. V. Rackham,[7] A. J. Burgasser,[12] X. Bonfils,[10] K. A. Collins,[13] B.-O. Demory,[14,15] G. Dransfield,[16,17] E. Ducrot,[18,19] A. Fukui,[20,6] M. Ghachoui,[2,21] Y. Gómez Maqueo Chew,[22] E. Jehin,[23] N. Narita,[20,24,6] P. P. Pedersen,[25,26] R. P. Schwarz,[13] G. Srdoc,[27] S. Yalçınkaya[28,29,2] and Z. Way[30]

Affiliations are listed at the end of the paper

Accepted 2026 April 2. Received 2026 March 6; in original form 2025 November 28

ABSTRACT

The Hidden Gems project searches the *TESS* data for additional planets transiting low-mass stars in confirmed systems. Our goal is to identify planet candidates that are below the detection threshold set by the SPOC and QLP pipelines using SHERLOCK, a specialized pipeline for robust detection and vetting of transit signals in *TESS* data. We present the discovery of two inner rocky planets in the TOI-237 and TOI-4336 A systems, validated with ground-based photometry from the TRAPPIST, SPECULOOS, ExTrA, and LCO facilities. TOI-237 c has a radius of $1.21 \pm 0.04\,R_\oplus$, orbits its mid-M host star every 1.74 d, and is close to a 3:1 mean-motion resonance with TOI-237 b. TOI-4336 A c has a radius of $1.17 \pm 0.06\,R_\oplus$, and orbits with a period of 7.58 d an M3.5 host star which is part of a hierarchical triple system. We performed model comparison to search for non-zero eccentricities, and found that the circular transit models are statistically favoured. Dynamical simulations show that both systems are in stable configurations, and the transit timing variations expected for the TOI-237 system are of the order of seconds. TOI-237 c and TOI-4336 A c join the high-interest population of warm likely super-Earths below the so-called radius valley. In particular, TOI-237 c is a good candidate for phase curve observations with *JWST*/MIRI thanks to the small radius of the host star and its short period.

Key words: planets and satellites: detection – planets and satellites: fundamental parameters – planets and satellites: terrestrial planets – stars: low-mass.

1 INTRODUCTION

Space-based surveys have unlocked the race to discover new exoplanets of all flavours. In particular, finding extrasolar worlds that represent the best laboratories for atmospheric investigation is one of the top priorities of professional planet hunters. In the past decade, *Kepler* (W. J. Borucki et al. 2010), *K2* (S. B. Howell et al. 2014), and *TESS* (G. R. Ricker et al. 2015) have detected thousands of exoplanet candidates, of which hundreds have been confirmed. These numbers reach more than 7000 candidates for 450 confirmed planets for *TESS* alone.[1] *TESS* objects of interest (TOIs) are publicly released after a periodic transit signal is found by the *TESS* science processing operations centre (SPOC), which is based on the *Kepler* pipeline (J. M. Jenkins et al. 2016). The SPOC pipeline produces calibrated data products, and extracts light curves and centroids for all targets with their associated uncertainties. It then searches for transiting candidates, labelled as threshold crossing events (TCEs), and performs a series of diagnostic tests to establish the level of confidence in the planetary nature of the signal. There are three requirements for a TCE to be promoted to a TOI status as explained in N. M. Guerrero et al. (2021): it must present at least two events; the significance of the events as evaluated by the multiple-event statistic should be above the threshold of 7.1; and it must pass a sequence of initial vetting tests. If all requirements are met, a TCE goes through a triage process to identify non-astrophysical signals, and a data validation report is produced with further vetting tests. Given the amount of data to comb through, a compromise was made between maximizing the number of true positives and minimizing the false positives in the *Kepler* and *TESS* SPOC pipelines. This opens the possibility of still finding new planet candidates by loosening the detection constraints with custom transit search pipelines.

★ E-mail: m.timmermans@bham.ac.uk

[1]Data from NASA Exoplanet Archive, 2024 4 June 4, https://exoplanetarchive.ipac.caltech.edu/

One such pipeline is SHERLOCK [2] (Searching for Hints of Exoplanets fRom Light curves Of spaCe-based seeKers), presented in F. J. Pozuelos et al. (2020) and M. Dévora-Pajares et al. (2024) and is now widely used to seek out extra planet candidates in the *TESS* data, as demonstrated in numerous discovery papers (e.g. L. Delrez et al. 2022; G. Dransfield et al. 2024); S. Zúñiga-Fernández et al. 2025). Making use of the full capabilities of SHERLOCK, we have first introduced the Hidden Gems project in M. Dévora-Pajares et al. (2024). This survey targets known transiting exoplanet systems orbiting low-mass stars to uncover additional planet candidates. Main-sequence stars with masses below 0.6 $M_\odot$ offer a unique opportunity to find small transiting planets with radii below 4 $R_\oplus$ thanks to the large planet-to-star surface ratios. Statistical population studies demonstrate that planets on short orbits around low-mass stars occur twice as frequently as for solar-type stars (e.g. C. D. Dressing & D. Charbonneau 2013; G. D. Mulders, I. Pascucci & D. Apai 2015; D. C. Hsu, E. B. Ford & R. Terrien 2020), and that about 20 per cent of mid-M dwarfs host compact multiple planetary systems (P. S. Muirhead et al. 2015). The presence of at least one confirmed planet in a system then increases the probability that convincing low signal-to-noise ratio (S/N) signals are produced by real planets. Transiting planets also offer the geometric advantage of already having a favourable orbital inclination to discover extra transiting planets (M. Gillon et al. 2011b). We limit our target list to K- and M-dwarf stars with $T_{\rm eff} < 5300$ K within 50 pc, corresponding to 181 planets in 119 unique systems. Our dynamical strategy relies on three steps: (1) perform the transit search with SHERLOCK on the available *TESS* sectors; (2) update the input data if new sectors become available to increase the S/N of putative signals, giving access to longer periods and smaller planets; and (3) periodically include newly discovered transiting systems in the target list.

We present in this paper the first planets discovered in the framework of the Hidden Gems project: TOI-237 c and TOI-4336 A c. These two systems were originally published as single-planet systems in W. C. Waalkes et al. (2021) and M. Timmermans et al. (2024), respectively. TOI-237 is a mid-M star with a radius of 0.21 ± 0.01 $R_\odot$ and a mass of 0.17 ± 0.04 $M_\odot$ for an effective temperature of 3226^{+47}_{-48} K. The newly discovered planet orbits its host star in 1.74 d, and has a radius of 1.206 ± 0.035 $R_\oplus$. It receives an irradiation of 16.0 ± 1.7 $S_\oplus$ which results in an equilibrium temperature of 515^{+11}_{-8} K. Similarly, TOI-4336 A is an M3.5 star part of a hierarchical triple system of M dwarfs and is the brightest component. The inner binary pair has an angular separation of 6.25 arcsec, and the two equal-mass stars are spatially resolved for photometric observations obtained with 1-m class telescopes. The host of the planetary system has a mass of 0.33 ± 0.01 $M_\odot$ and a radius of 0.31 ± 0.01 $R_\odot$ for an effective temperature of 3369^{+51}_{-57} K. TOI-4336 A c has a period of 7.59 d and receives an irradiation of 5.0 ± 0.6 $S_\oplus$ resulting in an equilibrium temperature of 378 ± 12 K. We find the planetary radius to be $1.165^{+0.061}_{-0.058}$ $R_\oplus$. Both of these new hot rocky planets are interesting candidates for atmospheric characterization. Detecting an atmosphere or the lack thereof around a hot rocky world would constrain formation and evolution scenarios for M dwarf hosts, known to experience very active stages during their lifetimes.

The structure of the paper is as follows: in Section 2, we describe how we performed the search for additional candidates with SHERLOCK. In Section 3, we characterize the host stars of the TOI-237 and TOI-4336 A systems. In Section 4, we detail the ground-based data obtained to confirm the existence of the planets, and report the global analyses made for both systems in Section 5. We explore the dynamics and possible transit timing variations (TTVs) in Section 7. Finally, we present our conclusions, and discuss the prospects for atmospheric and mass characterization in Section 8.

2 SEARCH FOR ADDITIONAL CANDIDATES

We used our custom transit search pipeline SHERLOCK to search for hidden periodic signals in the *TESS* 2-min pre-search data conditioning simple aperture photometry light curves. To achieve this, SHERLOCK is organized as a succession of six user-friendly modules described in detail in M. Dévora-Pajares et al. (2024). They can be summarized as follows: (1) light-curve acquisition from the NASA Mikulski Archive for Space Telescope using the LIGHTKURVE package (Lightkurve Collaboration 2018) and preparation of the data. The light curves are detrended with a bi-weight filter implemented by the WŌTAN package (M. Hippke et al. 2019) with varying window sizes. (2) The search for periodic signals is performed on the detrended light curves using a custom version of `Transit Least Square` (M. Hippke & R. Heller 2019). (3) A semi-automatic vetting of the signals is performed using the WATSON[3] package, similarly to the data validation module of the *TESS* pipeline, but also including a neural network vetting through WATSON-Net (M. Dévora-Pajares et al. 2025), based on all the metrics computed by WATSON. (4) The TRICERATOPS package (S. Giacalone et al. 2021) is used to statistically validate the planetary candidates. (5) Using the nested sampling algorithm of ALLESFITTER (M. N. Günther & T. Daylan 2019, 2021), a model is computed and the physical parameters of the system are estimated. (6) Ground-based follow-up campaigns are planned based on the ephemeris obtained from the Bayesian fit of the data.

2.1 TOI-237

TOI-237 (TIC 305048087) was observed three times by the *TESS* mission with short cadence observations, in Sectors 2, 29, and 69, as shown in Fig. 1. We limited our transit search to a maximum of five iterations, called 'runs', using 10 different window sizes for the detrended light curves. If a periodic signal is found above a certain S/N threshold, it is masked for the next iteration of the transit search. The search for candidates stops when the threshold is not met or when the user-set maximum number of runs is reached. We set the minimum S/N threshold for a signal to be accepted to 5 in order to include signals below the threshold of the *TESS* detections. In our initial analysis based only on Sector 2, we tested the use of a sliding Savitzky–Golay filter (SG, A. Savitzky & M. J. E. Golay 1964) that smooths the light curve before the bi-weight filter is applied. It is useful to enhance possible shallow signals, as was demonstrated in L. Delrez et al. (2022). This filter suppresses the high-frequency component of the noise, effectively reducing the point-to-point scatter ('local noise') at the cost of introducing correlation between adjacent data points. The caveat of this is that local artefacts might occasionally be confused with transit shapes. After inspecting the initial periodogram, we found no significant variability that warranted the use of the filter.

[2] https://github.com/franpoz/SHERLOCK

[3] https://github.com/PlanetHunters/watson

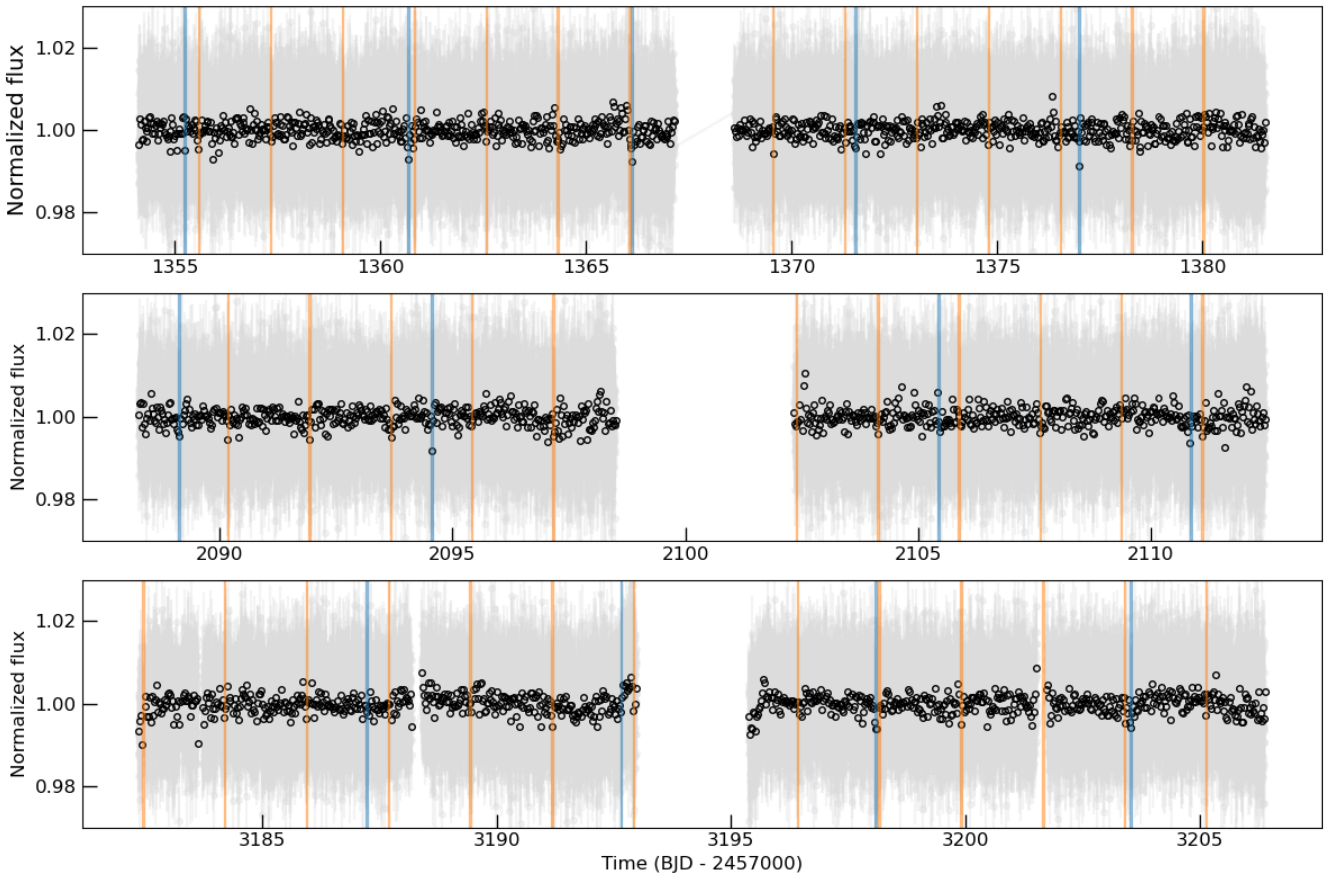

Figure 1. *TESS* 2-min cadence photometry of TOI-237 obtained with the *TESS* automatic aperture. Each of the panels shows the Sectors 2, 29, and 69, respectively. The gray points correspond to each measurement, and the black circles are binned by 36 minutes. TOI-237 b is highlighted in blue, and TOI-237 c (TIC 305048087.02) in orange.

We repeated the analysis without the filter, and as new sectors became available the S/N of the detection increased.

The initial search in Sector 2 identified TOI-237 b as a 5.43 d signal in all the detrended light curves of the first run, with a maximum S/N of 18 and a signal detection efficiency (SDE, M. Hippke & R. Heller 2019) of 15. The latter is used as a metric to assess whether a signal is significant enough to be distinguished from random noise fluctuations. A second signal at a period of 1.74 d was spotted in half of the detrended light curves, with a maximum S/N of 12 and an SDE of 5.9. We note these values are inflated due to the use of the SG filter. This second candidate, designated as TIC 305048087.02, corresponds to a period ratio of $\frac{P_b}{P_{cand}} \approx 3.1$, which is close to a 3:1 mean motion resonance. Surprisingly, in the combined analysis of Sectors 2 and 29, TIC 305048087.02 was the signal found in all the detrended light curves of the first run. It appeared to be the strongest signal in the data with an S/N of 11, and an SDE of 11, while TOI-237 b was found in the second run (S/N= 16 and SDE= 13) only in 8 out of the 10 detrended light curves. Finally, the last analysis including Sector 69 gave similar results: we confirmed that both signals were still present in the *TESS* data. TOI-237 b was found in the first run on 9 out of 10 detrended light curves (S/N= 8.9 and SDE= 22), and TIC 305048087.02 was identified in the second run in all of them (S/N= 7.9 and SDE= 25). For all three analyses, no flags were raised during the vetting of the candidate, not showing any odd/even differences or notable secondary events. Tests for possible centroids shifts and source offset were also negative, whilst the optical ghost check was passed. Upon analysis of the three available sectors, `WATSON-Net` yielded a score of 0.996 ± 0.006 for TOI-237 b and 0.73 ± 0.28 for the newly identified candidate. According to the classification criteria defined in M. Dévora-Pajares et al. (2025), these values place TOI-237 b within the validated planet regime and the new candidate within the likely planet regime, respectively. Therefore, the new candidate passed the vetting stage. We also performed the statistical validation procedure: the resulting null nearby false positive probability (NFPP) showed no hints of possible contamination from nearby sources, as expected since the target star is the only one in the *TESS* apertures. However, the false positive probability (FPP) = 0.73, was high enough to question the validity of the candidate. Given this value at this stage, the candidate could not be classified as validated or likely planet, and fell within the ambiguous region of the NFPP–FPP plane (S. Giacalone et al. 2021). Given the shallowness of the transit, we expected such a result. Although the Bayesian fit for the first sector provided us with a first set of ephemeris parameters, the uncertainties were initially too large to consider a targeted ground-based follow-up campaign. However, the short period and transit depth of $\sim$ 3 ppt of the candidate encouraged us to launch an exploratory filler program on the TRAPPIST-South (TRAnsiting Planets and

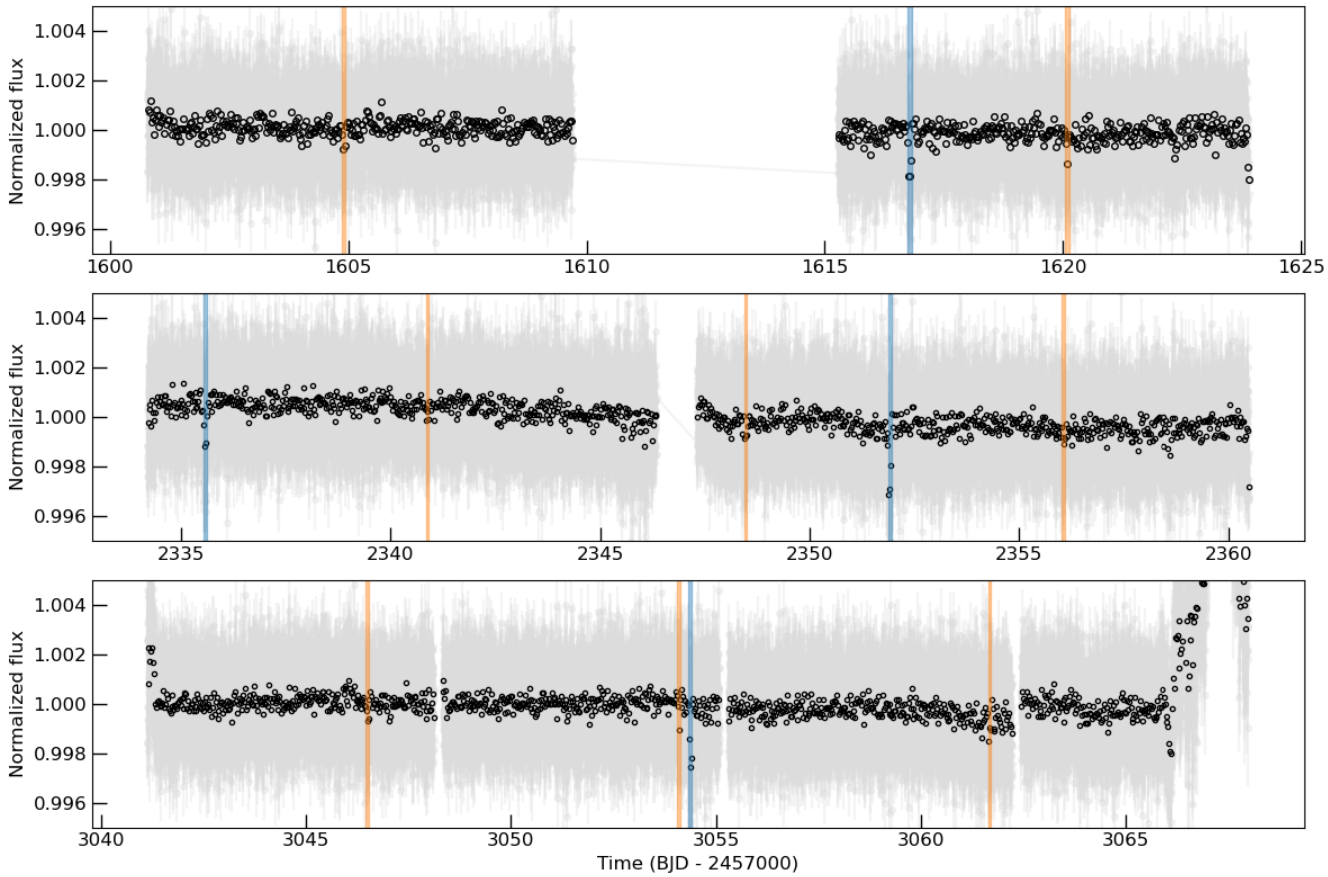

Figure 2. *TESS* 2-min cadence photometry of TOI-4336 A obtained with the same custom apertures as in M. Timmermans et al. (2024). Each of the panels shows the Sectors 11, 38, and 64, respectively. The gray points correspond to each measurement, and the black circles are binned by 36 minutes. TOI-4336 Ais highlighted in blue, and TOI-4336 A c (TIC 166184428.02) in orange.

PlanetesImals Small Telescope) telescope in 2021 (as described in Section 4.1). The later addition of Sectors 29 and 69 allowed for significant improvement in the precision on the ephemeris and matched two events in our ground-based data. This allowed us to move to a targeted approach rather than a blind search for our follow-up campaign.

2.2 TOI-4336 A

TOI-4336 A (TIC 166184428) was observed in three *TESS* sectors with short cadence: 11, 38, and 64, as shown in Fig. 2. The search for additional candidates was initially performed in the context of the discovery of TOI-4336 A b (M. Timmermans et al. 2024). The search for additional candidates and the selected parameters of the analysis are detailed in section 5.2 of the discovery paper. The signal of TOI-4336 A b was recovered in the first run of the analysis with an S/N of 18.70. The second candidate, denoted as TIC 166184428.02 was found in 4 out of the 10 detrended light curves of the second run with a period of 7.59 d. The S/N was close to the set threshold with a value of 5.35. The `WATSON-Net` vetting was also performed, yielding scores of 0.90 ± 0.18 for TOI-4336 A b and 0.62 ± 0.38 for TIC 166184428.02. The latter value indicates that the newly detected signal also satisfies the vetting criteria, exhibiting no problematic features and falling within the `WATSON-Net` uncertainty region. The statistical validation procedure was performed on TIC 166184428.02. The planet candidate obtained an FPP $= 0.42$ and an NFPP$= 0.42$, which is expected from a shallow transit and a contaminated aperture. From the TESS data alone, the candidate appears to be likely a false positive. The ephemeris obtained from the SHERLOCK pipeline allowed us to directly target observing windows with high chances of detection in the case of a true planet.

3 STELLAR CHARACTERIZATION

3.1 TOI-237 and TOI-4336 A

The stellar characterization of TOI-237 and TOI-4336 A is derived from publicly available astrometric, photometric, and spectral data. It employs advanced synthetic spectral fitting techniques to determine their fundamental parameters: effective temperature ($T_{\rm eff}$), metallicity ([M/H]), surface gravity ($\log g$), and radius. Our methodology, which will be detailed in Rojas-Ayala et al. (in preparation), differs from traditional spectral energy distribution (SED) fitting approaches for planet-hosting stars by incorporating four distinct synthetic spectral grids, as described below.

The photometric data for both stars were sourced from the 2MASS (Two Micron All-Sky Survey) and AllWISE (Wide-field Infrared Survey Explorer) catalogues (R. M. Cutri et al. 2003, 2021). Specifically, the 2MASS J-, H-, and K_s-band photometry, along with the AllWISE $W1$- and $W2$-band photometry, were utilized to constrain their SED in the near and mid-infrared regions.

Additionally, the *Gaia* Data Release 3 (DR3, Gaia Collaboration 2023) provided precise parallax measurements for both stars, which were critical for accurately estimating stellar radii, along with their *Gaia* XP spectrum. The *Gaia* XP spectra are absolute flux-calibrated, low-resolution ($R\sim$ 30–100) spectra, represented by a set of Hermite functions that approximate the continuous spectrum obtained from the BP and RP photometers (J. M. Carrasco et al. 2021; F. De Angeli et al. 2023; P. Montegriffo et al. 2023). In our analysis, instead of using the full *Gaia* XP spectrum for TOI-237 and TOI-4336, we utilized the GAIAXPY[4] package to reconstruct the spectra specifically for the RP photometer. This approach was chosen to avoid the low S/N issues at the blue end of the BP spectrum, which overlaps with the CaH feature characteristic of M dwarfs (see fig. 3 of J. M. Carrasco et al. 2021). For the fitting process, we focused on the 0.63–0.76 μm region of the RP spectrum. This spectral range was selected because it includes strong CaH and TiO absorption bands, which are particularly sensitive to metallicity (e.g. metallicity classes by S. Lépine, R. M. Rich & M. M. Shara 2007). Additionally, this choice helps to avoid potential artefacts at longer wavelengths that may arise from the spectrum reconstruction process using Hermite functions. These data sets were selected for their reliability, completeness, and relevance to the spectral characteristics of M dwarfs.

To derive the stellar parameters for both stars, we utilized the `species` PYTHON toolkit (T. Stolker et al. 2020), which facilitates the fitting of observed stellar data to a grid of synthetic spectra using Bayesian inference with nested sampling. Given that TOI-237 and TOI-4336 A are M dwarfs, we employed all suitable publicly available synthetic spectral grids that cover the M dwarf regime:

(i) BT-SETTL AGSS. These models offer a comprehensive treatment of dust formation and opacity in cool atmospheres, making them particularly suitable for M dwarfs (F. Allard, D. Homeier & B. Freytag 2012, 2013). They utilize the solar abundances from M. Asplund et al. (2009).

(ii) BT-SETTL CIFIST. Similar to the AGSS models (F. Allard et al. 2012, 2013) but updated with solar abundances from E. Caffau et al. (2011).

(iii) PHOENIX-ACES. A widely used model grid that includes detailed molecular line lists and enhanced opacity handling (T.-O. Husser et al. 2013).

(iv) SPHINX. A more recent model grid specifically designed for low-mass stars and brown dwarfs, with a focus on molecular opacity (A. R. Iyer et al. 2023).

The astrometric, photometric, and spectral data described above were fitted against these model grids to estimate the effective temperature, metallicity, surface gravity, and radius of each star. From these parameters, the star's mass and luminosity were subsequently derived using the estimated surface gravity, radius, and effective temperature using fundamental relations. The fitting process using the *species* toolkit was performed with priors that could be defined as either normal distributions or boundaries for uniform or log-uniform priors. To minimize degeneracies in the fitting, we employed the BP–RP colour and absolute K_s relationships from A. W. Mann et al. (2015). We note that the Gaia BP and RP magnitudes used in that work were synthetically generated from absolutely flux-calibrated spectra using pre-launch *Gaia* passbands (section 4.5 of A. W. Mann et al. 2015), and therefore do not correspond exactly to the calibrated *Gaia* DR3 photometric system. To ensure consistency with the photometric system underlying the empirical relations of A. W. Mann et al. (2015), we cross-matched their stellar sample with *Gaia* DR3 and computed the mean offsets between the synthetic magnitudes reported in that work and the observed DR3 values. We find systematic differences of $\Delta\mathrm{BP} = +0.166$ mag and $\Delta\mathrm{RP} = +0.012$ mag, which we apply as zero-point corrections to the *Gaia* DR3 magnitudes prior to using the BP–RP relation as an effective temperature and stellar radius prior. For the stellar mass prior, we used the absolute K_s relationship and its corresponding error from A. W. Mann et al. (2019). The *Gaia* DR3 parallax and its associated error were incorporated as a normal prior, while a boundary condition was set for the interstellar medium extinction (A_v). We then derived posterior probability distributions and Bayesian evidence for each of the synthetic spectral grids using the ULTRANEST[5] package (J. Buchner 2021).

To ensure robust estimates of the stellar parameters of TOI-237 and TOI-4336, we employed Bayesian model averaging (BMA) across all posterior probability distributions. BMA is a statistical technique that enhances predictions and provides reliable uncertainty estimates when fitting data to different synthetic spectral grids. Since multiple synthetic grids can explain the observational data with varying degrees of likelihood due to their differing physical assumptions, BMA allows us to simultaneously consider all four synthetic spectral grids described above. Each grid contributes to the final prediction, weighted by its relative evidence, which indicates how well the grid fits the data compared to the others. Our approach differs from other BMA-based SED-fitting techniques, such as ARIADNE (spectrAl eneRgy dIstribution bAyesian moDel averagiNg fittEr; J. I. Vines & J. S. Jenkins 2022), by including both spectral data (*Gaia* XP spectra) and photometric data, and by utilizing grids specifically tailored for the M dwarf regime, such as BT-SETTL AGSS, BT-SETTL CIFIST, and SPHINX, which are not available in ARIADNE. The BMA results for TOI-237 and TOI-4336 Are presented in Table 1.

Table 1. Stellar characterization of TOI-237 and TOI-4336 A.

Parameters	TOI-237	TOI-4336 A
Luminosity $L_\star$ ($L_\odot$)	0.0041 ± 0.0003	$0.0115^{+0.0008}_{-0.0010}$
Radius $R_\star$ ($R_\odot$)	$0.2056^{+0.0047}_{-0.0067}$	$0.3126^{+0.0095}_{-0.0070}$
Mass $M_\star$ ($M_\odot$)	$0.1698^{+0.0385}_{-0.0350}$	$0.2853^{+0.0438}_{-0.0356}$
Surface gravity $\log g_\star$ (cgs)	$5.0494^{+0.0865}_{-0.0923}$	$4.9107^{+0.0502}_{-0.0621}$
Effective temperature $T_{\rm eff}$ (K)	3226^{+47}_{-48}	3369^{+51}_{-57}
Metallicity [Fe/H] (dex)	$-0.3443^{+0.6245}_{-0.3964}$	$0.2090^{+0.2323}_{-0.3337}$
Parallax π (mas)	$26.1213^{+0.0346}_{-0.0438}$	$44.5389^{+0.0400}_{-0.0505}$

3.2 Spectroscopic classification of TOI-237

In addition to analysis of publicly available data, we also acquired a moderate-resolution spectrum of TOI-237 on 2025 December 3 using the Goodman Spectrograph (J. C. Clemens, J. A. Crain & R. Anderson 2004) on the SOAR (Southern Astrophysical Research) telescope via the AEON queue. Conditions were clear with 1.3 arcsec seeing. We used the red camera with the 400 lines mm^{-1} grating, the 1 arcsec slit, and 2 × 2 binning to gather

[4]DOI v2.1.2: 10.5281/zenodo.11617977, https://gaia-dpci.github.io/GaiaXPy-website/

[5]https://johannesbuchner.github.io/UltraNest/

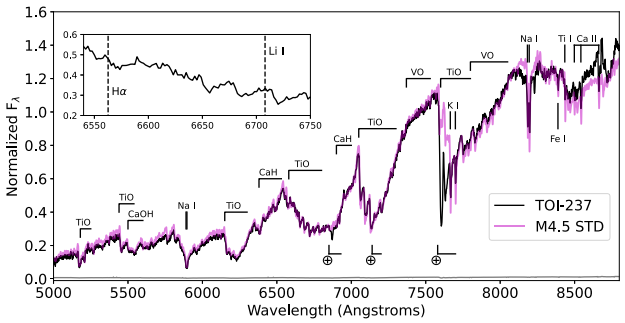

Figure 3. Optical spectrum of TOI-237 (black line) normalized at 7100 Å, compared to its best-fitting spectral template, a combination M4 and M5 dwarf types (A. Y. Kesseli et al. 2017, magenta line). Key molecular and atomic spectral features are labelled, as are uncorrected telluric features (⊕). The inset box shows a close-up of the 6500–6750 Å region encompassing Hα and Li I lines.

two 120-s exposures, yielding spectral coverage of 0.5–0.9 μm at a resolving power of $R \approx 1000$. Standard flat-field and arc-lamp calibrations were collected immediately before and after the science sequence. The spectrophotometric standard HR 9087 was observed during the same night for flux calibration, and no explicit telluric correction was applied. Data reduction was performed with PYPEIT (J. Prochaska et al. 2020; J. X. Prochaska et al. 2020), following standard procedures. The final spectrum has a median signal-to-noise ratio of S/N ≈ 100 at 7500 Å.

The reduced spectrum is shown in Fig. 3, and shows features typical of mid-M dwarfs, including molecular absorption from TiO, CaH, and CaOH, and various atomic line features. Using the KASTREDUX package,[6] we compared the spectrum to Sloan Digital Sky Survey templates from A. Y. Kesseli et al. (2017) and found a best-fitting comparison as an average of M4 and M5 spectral standards, while spectral classification indices from I. N. Reid, S. L. Hawley & J. E. Gizis (1995); J. E. Gizis & I. N. Reid (1997); and S. Lépine, R. M. Rich & M. M. Shara (2003); and F. C. Riddick, P. F. Roche & P. W. Lucas (2007) indicate types spanning M3.5–M4.5. We therefore adopt a classification of M4±1 for TOI-237, which is consistent with the mass, radius, and temperature inferred from our spectrophotometric analysis (e.g. an M4±1 dwarf has a $T_{\rm eff} = 3200\pm160$ K; M. J. Pecaut & E. E. Mamajek 2013). We computed the ζ metallicity index (S. Lépine et al. 2007, 2013) of 1.011±0.004, corresponding to a metallicity of [Fe/H] = +0.02±0.20 based on the empirical calibration of A. W. Mann et al. (2013), within the broader uncertainty range of the spectrophotometric analysis. We find no evidence of significant Hα emission, suggesting an age $\gtrsim$4.5 Myr (A. A. West et al. 2008).

4 GROUND-BASED PHOTOMETRIC OBSERVATIONS

We triggered follow-up observing campaigns with ground-based facilities to confirm or rule out the existence of the additional planetary candidates found in the TOI-237 and TOI-4336 A systems.

[6] https://github.com/aburgasser/kastredux

4.1 TRAPPIST-South

TRAPPIST-South (E. Jehin et al. 2011; M. Gillon et al. 2011a) is a 0.6-m telescope hosted by ESO La Silla Observatory in Chile and operational since 2010. This Ritchey-Chrétien telescope with $F/8$ is fully robotic and equipped with an FLI ProLine PL3041-BB camera with a 2K×2K back-illuminated CCD. This results in a field of view of 22 arcmin×22 arcmin thanks to a pixel scale of 0.64 arcsec pixel^{-1}. The TRAPPIST-South telescope was used to confirm the existence of TOI-237 c by performing an informed search for a full observing season of TOI-237 using the observation plans provided by SHERLOCK. This was part of the filler program of the Exo-TRAPPIST project dedicated to the observation of Hidden Gems candidates, totaling 43 nights and over 175 h of observation of TOI-237. The observations were all obtained in the $I+z$ filter to maximize the S/N with exposure times of 120 s (summarized in Table 2). The data reduction and analysis was performed using a dedicated pipeline designed with the PROSE package (L. J. Garcia et al. 2021, 2022). The nights were processed independently, with comparison stars and an optimal apertures selected to reduce the white noise in the individual light curves. To evaluate whether the planet would be recovered in our observations, we computed the phase coverage as for periods between 0 and 8 d with intervals of 0.001 d, as shown in Fig. 4. The percentage of phase coverage represents how much of the orbit at a certain orbital period is explored by our observations. We find that we reach a phase coverage of ∼80 per cent at a period of $P = 5.15$ d, and ∼98 per cent for $P = 1.74$ d. We have thus sampled efficiently the phases of potential inner planets to TOI-237 b. In doing so, we recover the transit signal of TOI-237 c at the predicted ephemeris and do not find any hints of additional transit signals by eye.

4.2 SPECULOOS-South

The SPECULOOS-Southern Observatory (SSO, L. Delrez et al. 2018; D. Sebastian et al. 2021) is located at ESO's Paranal Observatory in Chile. It is comprised of four identical 1.0-m class telescopes in a Ritchey–Chrétien configuration with $F/8$. Each are equipped with a thermoelectrically cooled Andor iKon-L camera with a deep-depletion CCD chip of 2K×2K pixels. The pixel scale of 0.35 arcsec pixel^{-1} provides a total field of view of 12 arcmin × 12 arcmin. We used the SPECULOOS-South telescopes to observe transits of TOI-237 b, TOI-237 c, and TOI-4336 A c. We observed TOI-237 on 2022 October 13 simultaneously in three filters (Sloan-g', $I+z$, and the custom zYJ) with exposures of 150, 13, and 7 s, respectively. On that night, we observed a full transit of TOI-237 c and the egress of TOI-237 b. Observing in the zYJ-band was made possible by the SPIRIT (SPeculoos InfraRed Imager for Transits) camera, a new near-infrared camera that was being tested on SSO/Callisto at the time (P. P. Pedersen et al. 2024). A full transit of TOI-237 b was obtained on 2022 November 9 in the $I+z$ filter with exposures of 13 s. We observed simultaneously in the Sloan-r' and $I+z$ filters the transit of TOI-237 c on 2022 October 20 with exposure times of 120 and 16 s, respectively. Finally, we obtained two new transits in the $I+z$ filter on 2022 October 27 and November 10 with exposure times of 16 and 13 s. All the transit observations of TOI-237 b and c are summarized in Table 2, and of TOI-4336 A c in Table 3. A transit of TOI-4336 A c was obtained in the Sloan-r' filter simultaneously on two telescopes with exposure times of 10 s. All the data reduction and photometric extraction was done with the same custom pipeline used for the TRAPPIST-South data, built with the PROSE package.

Table 2. Summary of the ground-based follow-up observations obtained for the TOI-237 system.

Observatory	Filter	Date	Coverage	Exposure (s)	FWHM (arcsec)	Aperture (arcsec)	Measurements
Planet b							
ExTrA (T2)	1.21 μm	2021 July 13	Full	60	1.48	4	134
ExTrA (T2)	1.21 µm	2021 Aug 20	Full	60	1.32	4	129
ExTrA (T3)	1.21 µm	2021 Aug 20	Full	60	1.25	4	129
ExTrA (T2)	1.21 µm	2021 Oct 19	Full	60	1.64	4	203
ExTrA (T3)	1.21 µm	2021 Oct 19	Full	60	1.45	4	203
ExTrA (T2)	1.21 µm	2021 Oct 30	Full	60	1.63	4	216
TRAPPIST-South	$I+z$	2021 Oct 30	Full	120	2.63	4.87	153
TRAPPIST-South	$I+z$	2021 Dec 07	Full	120	2.66	4.53	92
TRAPPIST-South	$I+z$	2022 Sept 21	Full	120	2.42	4.48	184
ExTrA (T2)	1.21 µm	2022 Oct 02	Full	60	1.30	4	150
TRAPPIST-South	$I+z$	2022 Oct 02	Full	120	3.60	5.77	103
SSO/Europa	Sloan-g'	2022 Oct 13	Egress	150	1.46	1.61	185
SSO/Callisto	zYJ	2022 Oct 13	Egress[a]	7	2.02	1.21	4012
SSO/Io	$I+z$	2022 Oct 13	Egress	13	1.82	3.36	1308
SSO/Io	$I+z$	2022 Nov 02	Full	13	1.77	2.84	757
TRAPPIST-South	$I+z$	2022 Nov 09	Full	120	2.91	3.93	123
ExTrA (T2)	1.21 µm	2022 Nov 09	Full	60	1.28	4	150
Planet c							
TRAPPIST-South	$I+z$	2021 Oct 29	Full	120	2.50	3.90	90
TRAPPIST-South	$I+z$	2021 Nov 05	Full	120	2.71	5.34	75
TRAPPIST-South	$I+z$	2021 Nov 19	Full	120	2.62	4.33	83
TRAPPIST-South	$I+z$	2021 Nov 26	Full	120	3.17	5.20	110
TRAPPIST-South	$I+z$	2021 Dec 03	Full	120	2.83	4.79	109
TRAPPIST-South	$I+z$	2021 Dec 17	Egress[b]	120	3.02	4.47	78
TRAPPIST-South	$I+z$	2022 May 14	Full	120	1.37	3.75	80
TRAPPIST-South	$I+z$	2022 June 11	Full	120	2.87	3.88	137
TRAPPIST-South	$I+z$	2022 Aug 25	Full	120	1.93	3.09	141
TRAPPIST-South	$I+z$	2022 Sept 01	Full	120	2.33	3.72	146
TRAPPIST-South	$I+z$	2022 Sept 15	Full	120	2.25	3.60	215
TRAPPIST-South	$I+z$	2022 Sept 22	Full	120	2.17	4.01	134
TRAPPIST-South	$I+z$	2022 Sept 29	Full	120	2.24	4.15	158
SSO/Europa	Sloan-g'	2022 Oct 13	Full	150	1.46	1.61	185
SSO/Callisto	zYJ	2022 Oct 13	Full[a]	7	2.02	1.21	4012
SSO/Io	$I+z$	2022 Oct 13	Full	13	1.82	3.36	1308
TRAPPIST-South	$I+z$	2022 Oct 13	Full[b]	120	3.11	4.98	188
SSO/Europa	Sloan-r'	2022 Oct 20	Full	120	1.27	2.67	110
SSO/Io	$I+z$	2022 Oct 20	Full	16	1.51	3.55	530
TRAPPIST-South	$I+z$	2022 Oct 20	Full	120	2.42	4.47	105
SSO/Io	$I+z$	2022 Oct 27	Full	16	1.67	3.09	369
TRAPPIST-South	$I+z$	2022 Oct 27	Full	120	2.62	4.19	122
SSO/Io	$I+z$	2022 Nov 10	Full	13	1.23	2.59	473

Notes. [a] The light curve is too noisy and was not included in the global analysis.
[b]The observation is affected by bad weather and was not included in the global analysis.

4.3 ExTrA

ExTrA (Exoplanets in Transits and their Atmospheres, X. Bonfils et al. 2015) is a low-resolution near-infrared (0.85–1.55 µm) multi-object spectrograph fed by three 60-cm telescopes located at La Silla Observatory in Chile. Six transits of TOI-237 b were observed using one or two of the ExTrA telescopes. We used 8 arcsec diameter aperture fibres and the low-resolution mode ($R \sim 20$) of the spectrograph, with an exposure time of 60 s. Five fibres are positioned in the focal plane of each telescope to select light from the target and four comparison stars. The resulting ExTrA data were analysed using custom data reduction software.

4.4 LCO-CTIO-1m0

Two full transits of TOI-4336 A c were observed with LCO-CTIO-1m0 (T. M. Brown et al. 2013) on 2024 March 3 and April 9 at Cerro Tololo Interamerican Observatory in Chile. Both transits were carried out in the Sloan-i' filter with an exposure time of 22 s. The telescope is equipped with 4096 × 4096 Sinistro cameras with a pixel scale of 0.389 arcsec pixel^{-1}, resulting an FOV of 26 arcmin × 26 arcmin.is not a The transits were scheduled using the *TESS* Transit Finder based on the TAPIR software (E. Jensen 2013), and the science data were calibrated with the standard LCOGT BANZAI (C. McCully et al. 2018) pipeline. The photometric extraction was performed with the PROSE pipeline.

4.5 LCO-HAL-2m0/MuSCAT3

A full transit of TOI-4336 A c was observed with LCO-HAL-2m0 on UT 2024 June 02 at Haleakala Observatory in Hawaii. The telescope is equipped with with the MuSCAT3 (Multicolor Simultaneous Camera for studying Atmospheres of Transiting exoplanets) multiband imager (N. Narita et al. 2020). The transit

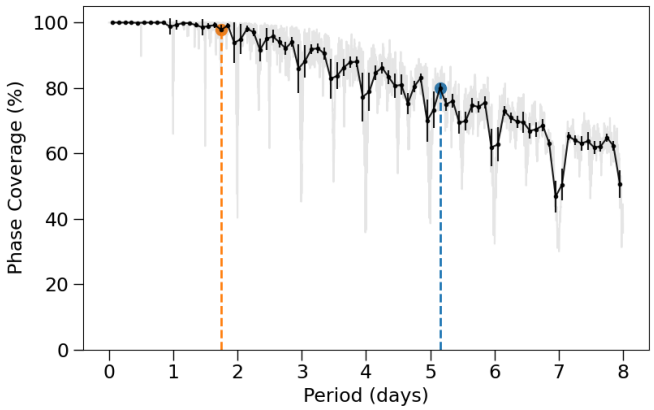

Figure 4. Phase coverage from the observations of TOI-237 obtained with TRAPPIST-South described in Section 4.1. The light grey line represents the percentage of phase covered for each orbital period from 0.001 to 8 d with steps of 0.001 d. The black line shows the phase coverage for periods binned by 2.4 h. The dashed orange line corresponds to $P = 1.74$ d, the period of TOI-237 c, at which we find a coverage of ∼98 per cent. The blue line corresponds to $P = 5.15$ d at which a coverage of ∼80 per cent is reached.

was carried out simultaneously with the Sloan-g', -r', -i', and Pan-STARRS-z_s filters. The data were calibrated with the standard LCOGT BANZAI pipeline. The photometric extraction was performed with the PROSE pipeline.

5 GLOBAL PHOTOMETRIC ANALYSIS

We performed a global analysis of the all the available photometric data of both systems using `allesfitter` (M. N. Günther & T. Daylan 2019, 2021), a PYTHON-based inference package. This includes all the data published in W. C. Waalkes et al. (2021) and M. Timmermans et al. (2024). By doing so, our aim is to provide stronger constraints on the estimations of the physical parameters of the systems thanks to the combination of all the available statistical information. `allesfitter` allows to build transit models using the ELLC package (P. F. L. Maxted 2016), while including the modelling of astrophysical noise sources such as flares, spots, and variability. Correlated noise can be accounted for using splines, or Gaussian processes (e.g. C. E. Rasmussen & C. K. I. Williams 2006) implemented with the CELERITE package (D. Foreman-Mackey et al. 2017; D. Foreman-Mackey 2018). We made use of the nested sampling algorithm implemented by the DYNESTY package (J. S. Speagle 2020) in `allesfitter` to perform model comparison. This sampling method allows for the computation of the Bayesian evidence for each model, and we then calculate the Bayes Factor to determine whether one model is statistically favoured over another (R. E. Kass & A. E. Raftery 1995).

The data sets are separated according to their exposure times, filters and instruments. Given the large gap in the TRAPPIST-South data between the transit of TOI-237 b obtained in 2019 and the rest, we treated them as separate instruments. Because we include all the available photometry in our analysis, we chose wide uniform priors on the fitted planetary parameters (the radius ratio $R_p/R_\star$, the scale parameter $(R_p + R_\star)/a$, the cosine of the orbital inclination $\cos i$, the epoch T_0, and the orbital period P). The prior distributions used in the modelling of the TOI-237 and TOI-4336 A systems can be found in Tables 4 and 5, respectively. The derived parameters appearing in the tables are: the radius of the planet R_p, the semimajor axis a, the orbital inclination i, the total transit duration T_{1-4}, the equilibrium temperature T_{eq} defined with an albedo of 0.3, the transit depth δ corresponding to the minimum of the stellar flux, and the impact parameter b.

The photometric observations span a range of different filters. We obtained the quadratic limb-darkening coefficients u_1 and u_2 from A. Claret, P. H. Hauschildt & S. Witte (2012) and A. Claret (2018) for ground-based data and *TESS*, respectively, except for the ExTrA 1.2 µm and Sloan-z_s filters for which we used the PYLDTK package (H. Parviainen & S. Aigrain 2015) based on the PHOENIX model atmospheres (T.-O. Husser et al. 2013). They are given in Tables A1 and A2. We converted u_1, u_2 into q_1, q_2 with the parametrization presented in D. M. Kipping (2013), as required by `Allesfitter`.

In the case of the TOI-4336 A system, we include a free dilution factor with a wide uniform prior for *TESS* where both TOI-4336 A and B are included in the aperture to account for possible blended faint additional stars. In the case of the LCO/MuSCAT3 data, the defocusing of the observations produced a slight blending of the wings of the two stars' point spread functions. We include a smaller dilution factor to account for this effect. The dilution factors obtained for the global analysis of TOI-4336 A b and c are given in Table 6.

Finally, we use GPs with a *Matérn 3/2* kernel to model stellar variability and any correlated noise. In the first instance, we place wide uniform priors on the GP hyperparameters (σ, the amplitude scale, and ρ, the length scale). We then use the fitted hyperparameters of the first analysis as priors for the subsequent analyses to reduce the computational time for the different models. A flaring event is present in the simultaneous light curves of TOI-4336 A c obtained on 2024 June 1 with MuSCAT3. This initially caused the GP to overfit the data for the Sloan-i' filter. Modelling the flare is beyond the scope of this work therefore, we opted to simply mask it out.

Table 3. Summary of the ground-based follow-up observations obtained for the TOI-4336 A system.

Observatory	Filter	Date	Coverage	Exposure (s)	FWHM (arcsec)	Aperture (arcsec)	Measurements
Planet c							
LCO-CTIO−1m0	Sloan-i'	2024 Mar 02	Full	22	1.74	2.34	262
SSO/Io	Sloan-r'	2024 Apr 09	Full	10	1.70	2.72	1041
SSO/Callisto	Sloan-r'	2024 Apr 09	Full	10	1.00	3.26	1251
LCO-CTIO−1m0	Sloan-i'	2024 Apr 09	Full	22	1.32	3.42	263
LCO-HAL−2m0/MuSCAT3	Sloan-g'	2024 June 01	Full	144	3.02	3.08	71
LCO-HAL−2m0/MuSCAT3	Sloan-r'	2024 June 01	Full	17	2.67	3.08	480
LCO-HAL−2m0/MuSCAT3	Sloan-i'	2024 June 01	Full	12	2.84	3.08	611
LCO-HAL−2m0/MuSCAT3	PanSTARRS-zs	2024 June 01	Full	10	2.59	2.46	804

Table 4. Properties of TOI-237 system.

Parameters	Values		Priors		Source
	Planet b	Planet c	Planet b	Planet c	
$R_p/R_\star$	0.0601 ± 0.0015	0.0526 ± 0.0013	$\mathcal{U}(0.01, 0.10)$	$\mathcal{U}(0.01, 0.10)$	Fitted
$(R_\star + R_p)/a$	$0.02993^{+0.00112}_{-0.00071}$	$0.0640^{+0.0025}_{-0.0017}$	$\mathcal{U}(0.01, 0.05)$	$\mathcal{U}(0.01, 0.08)$	Fitted
$\cos i$	$0.0064^{+0.0037}_{-0.0038}$	$0.0150^{+0.0082}_{-0.0086}$	$\mathcal{U}(0.00, 0.04)$	$\mathcal{U}(0.00, 0.04)$	Fitted
Epoch, T_0 (BJD-TDB$_{2450000}$)	$8697.72080^{+0.00047}_{-0.00045}$	$9540.35059^{+0.00023}_{-0.00024}$	$\mathcal{U}(8697.70, 8697.74)$	$\mathcal{U}(9540.32, 9540.38)$	Fitted
Orbital period, P (d)	$5.43613914^{+0.0000028}_{-0.0000029}$	$1.74486147^{+0.0000013}_{-0.0000010}$	$\mathcal{U}(5.4, 5.5)$	$\mathcal{U}(1.7, 1.8)$	Fitted
Planet radius, R_p ($R_\oplus$)	1.379 ± 0.040	1.206 ± 0.035	–	–	Derived
Semimajor axis, a (au)	$0.0346^{+0.0010}_{-0.0013}$	$0.0160^{+0.0005}_{-0.0006}$	–	–	Derived
Orbital inclination, i (deg)	89.63 ± 0.22	$89.14^{+0.49}_{-0.47}$	–	–	Derived
Transit duration, T_{1-4} (h)	$1.213^{+0.015}_{-0.014}$	0.827 ± 0.010	–	–	Derived
Equilibrium temperature, T_{eq} (K)	350^{+7}_{-5}	515^{+11}_{-8}	–	–	Derived
Transit depth$_{TESS}$, δ (ppt)	$4.12^{+0.20}_{-0.21}$	$3.14^{+0.17}_{-0.15}$	–	–	Derived
Impact parameter, b	$0.22^{+0.12}_{-0.13}$	$0.25^{+0.12}_{-0.14}$	–	–	Derived
Insolation flux, S_p ($S_\oplus$)	3.4 ± 0.4	16.0 ± 1.7	–	–	Derived

Table 5. Properties of TOI-4336 A system.

Parameters	Values		Priors		Source
	Planet b	Planet c	Planet b	Planet c	
$R_p/R_\star$	$0.0580^{+0.0012}_{-0.0011}$	0.0341 ± 0.0015	$\mathcal{U}(0.01, 0.10)$	$\mathcal{U}(0.01, 0.10)$	Fitted
$(R_\star + R_p)/a$	$0.01923^{+0.00094}_{-0.00078}$	$0.03127^{+0.00165}_{-00141}$	$\mathcal{U}(0.01, 0.05)$	$\mathcal{U}(0.01, 0.05)$	Fitted
cos$i$	$0.0095^{+0.0016}_{-0.0014}$	0.0088 ± -0.0046	$\mathcal{U}(0.00, 0.04)$	$\mathcal{U}(0.00, 0.04)$	Fitted
Epoch, T_0 (BJD-TDB$_{2450000}$)	9335.57275 ± 0.00046	9333.29293 ± -0.00200	$\mathcal{U}(9335.54, 9335.60)$	$\mathcal{U}(9333.26, 9333.32)$	Fitted
Orbital period, P (d)	16.336350 ± -0.000017	$7.587270^{+0.000015}_{-0.000013}$	$\mathcal{U}(16.0, 16.5)$	$\mathcal{U}(7.55, 7.62)$	Fitted
f_c	0 (fixed)	$0.025^{+0.327}_{-0.329}$	–	$\mathcal{U}(-1, 1)$	Fitted
f_s	0 (fixed)	$-0.067^{+0.188}_{-0.185}$	–	$\mathcal{U}(-1, 1)$	Fitted
Planet radius, R_p ($R_\oplus$)	$2.044^{+0.069}_{-0.065}$	$1.165^{+0.061}_{-0.058}$	–	–	Derived
Semimajor axis, a (au)	$0.0802^{+0.0040}_{-0.0042}$	0.0481 ± 0.0027	–	–	Derived
Orbital inclination, i (deg)	$89.46^{+0.08}_{-0.09}$	$89.50^{+0.26}_{-0.27}$	–	–	Derived
Eccentricity, e	0 (fixed)	$0.093^{+0.160}_{-0.069}$	–	–	Derived
Transit duration, T_{1-4} (h)	$2.087^{+0.020}_{-0.021}$	$1.766^{+0.070}_{-0.034}$	–	–	Derived
Equilibrium temperature, T_{eq} (K)	293 ± 8	378 ± 12	–	–	Derived
Transit depth$_{undil,TESS}$, δ (ppt)	$3.93^{+0.26}_{-0.24}$	$1.31^{+0.47}_{-0.35}$	–	–	Derived
Impact parameter, b	0.52 ± 0.06	$0.29^{+0.16}_{-0.15}$	–	–	Derived
Insolation flux, S_p ($S_\oplus$)	1.8 ± 0.2	5.0 ± 0.6	–	–	Derived

Table 6. Dilution parameters obtained in the global analysis of the TOI-4336 A system.

Parameters	Values	Priors
Dil. *TESS*	0.480 ± -0.026	$\mathcal{U}(-1,1)$
Dil. TRAPPIST-South	$0.581^{+0.084}_{-0.086}$	$\mathcal{U}(-1,1)$
Dil. MuSCAT3 (Sloan-g')	$-0.02^{+0.21}_{-0.22}$	$\mathcal{U}(-0.4,0.4)$
Dil. MuSCAT3 (Sloan-r')	-0.00 ± -0.20	$\mathcal{U}(-0.4,0.4)$
Dil. MuSCAT3 (Sloan-i')	-0.04 ± 0.18	$\mathcal{U}(-0.4,0.4)$
Dil. MuSCAT3 (PanSTARRS-zs)	$-0.17^{+0.16}_{-0.14}$	$\mathcal{U}(-0.4,0.4)$

5.1 Model comparison

For both systems, we performed an initial analysis with a one-planet circular fit. We then tested two-planet fits with a combination of circular and eccentric orbits: (1) both planets have circular orbits (we note it 2p–1c2c for convenience), (2) planet b is circular and planet c is eccentric (2p–1c2e), (3) planet b is eccentric and planet c is circular (2p–1e2c), and (4) both planets are eccentric (2p–1e2e). An eccentric orbit is parametrized in `allesfitter` by $f_c = \sqrt{e}\cos\omega$ and $f_s = \sqrt{e}\sin\omega$, where e is the eccentricity and ω the argument of periastron. For all eccentric fits, we chose wide uniform priors $\mathcal{U}(-1, 1)$ for f_c and f_s. We computed the Bayes Factor $\Delta \ln(Z) = \ln(Z) - \ln(Z_0)$ by comparing the model evidences

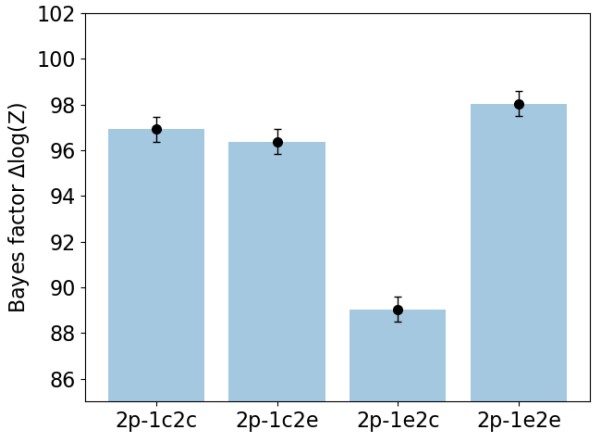

Figure 5. Bar plot representing the Bayes factor of the tested models for the TOI-237 system. The null hypothesis is taken as a one-planet circular fit, the other models are two-planet fits: two circular orbits, planet b circular and planet c eccentric, the inverse, and two eccentric orbits.

Table 7. Eccentricities e and arguments of periastron ω obtained in the model comparison for the two-planet fits of the TOI-237 system.

Model	Parameter	
	e	ω (deg)
2p-1c2e (TOI-237 c)	$0.101^{+0.206}_{-0.075}$	$198.83^{+137.46}_{-133.46}$
2p-1e2c (TOI-237 b)	$0.082^{+0.162}_{-0.060}$	$180.58^{+124.59}_{-126.85}$
2p-1e2e (TOI-237 b)	$0.095^{+0.179}_{-0.070}$	$175.37^{+70.07}_{-113.21}$
2p-1e2e (TOI-237 c)	$0.088^{+0.176}_{-0.066}$	$188.90^{+121.89}_{-127.48}$

given by ln$Z$ to the one of the null hypothesis given by ln(Z_0). The null hypothesis represents the simplest model capable of explaining the data, and we chose it to be the one-planet circular fit in the analysis of both systems. R. E. Kass & A. E. Raftery (1995) give $\Delta \log(Z) > 3$ as the limit for strong evidence of one model. We also note that a Bayes factor indicating evidence in favour of one model is primarily suggestive. In our case, observational constraints on the architecture of the system could also be obtained from radial velocity (RV) measurements as they are sensitive to the eccentricity and orbital angles. However, for this study we did not have access to such measurements, thus we relied on the model comparison approach to determine if the orbits appear eccentric. The results are illustrated as bar plots in Fig. 5.

For the TOI-237 system, we find that all two-planet scenarios are very strongly statistically favoured ($\Delta \ln(Z) > 85$). Comparing their Bayesian evidences assuming circular and eccentric orbits, the model including eccentric orbits for both planets is the most likely. Although, compared to the other two-planet models, 2p–1e2e is not strongly favoured against 2p–1c2c and 2p–1c2e with Bayes factors of 1 and 2, respectively. We note that the 2p–1e2c model presents the smallest evidence and is thus ruled out. The eccentricities and arguments of periastron found for each scenario are given in Table 7. All models are consistent with a zero eccentricity at the 1σ level. We do not consider this to be a significant detection of eccentricity. To comply with the basic principle of model comparison (Occam's razor principle), i.e. the simplest model able to explain the data should be favoured, we select the two-planet circular fit as the most likely outcome. The

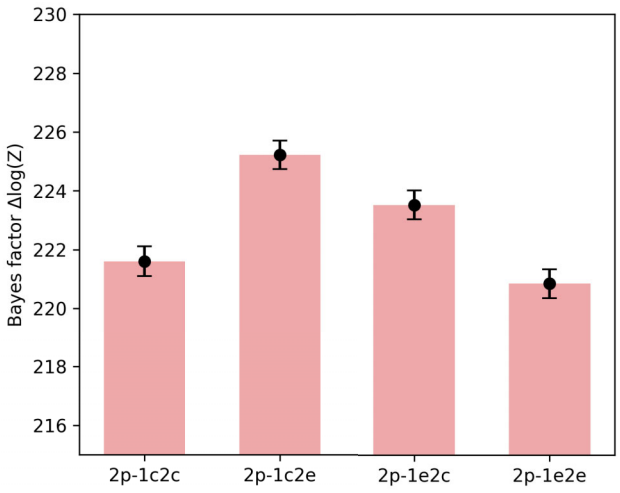

Figure 6. Bar plot representing the Bayes factor of the tested models for the TOI-4336 A system. The null hypothesis is taken as a one-planet circular fit, the other models are two-planet fits: two circular orbits, planet b circular and planet c eccentric, the inverse, and two eccentric orbits.

fitted and derived parameters of the preferred model are given in Table 4, and the phase-folded light curves and associated models are shown in Figs B1 and B2.

Similarly, the two-planet fits are also strongly statistically favoured compared to the null hypothesis in the case of the TOI-4336 A system, with $\Delta \ln(Z) > 220$, as shown in Fig. 6. The model evidences are more contrasted than in the previous case, and we find that the 2p–1c2e model is the most strongly favoured in this model comparison analysis with a $\Delta \ln(Z) = 3.6$. We note that the eccentricity found for planet c is not very well constrained and is also consistent with zero eccentricity at the 1σ level. We show the phase-folded light curves and individual model in Figs B3 and B4, as well as the fitted and derived parameters for the adopted model in Table 5.

6 PLANET VALIDATION

6.1 TOI-237 c

In the absence of a mass measurement, validating the planetary nature of a transiting object is typically done by evaluating and discarding the possibilities of false positives. From our photometric datasets, we performed the two tests designed to identify eclipsing binaries or blended scenarios by a background object: chromatic variations of the transit depth, and odd/even transit discrepancies. In the case of TOI-237 c, no odd/even differences were observed in the *TESS* light curves or our ground-based TRAPPIST-South data. To test for chromaticity, we performed a new global analysis with `Allesfitter` following the same method described in Section 5 but adding a free dilution term per wavelength band. The bands considered here are Sloan-g' ($\sim 400-550$ nm), Sloan-r' ($\sim 550-700$ nm), Ic ($\sim 720-880$ nm), $I+z$($\sim 750-1000$ nm), and the narrow band at 1.41 μm (6 nm wide) of the ExTrA telescope. We used a uniform prior between -1 and 1, and kept it fixed to 0 for the *TESS* data to serve as reference. For all filters but one, we obtained results consistent within 1σ with a dilution of 0. These are given in Table 8. The inconsistency of the Sloan-g' band is likely attributed to the too large

Table 8. Dilution parameters obtained in the chromaticity check of TOI-237 c.

Parameters	Values	Priors
Dil. *TESS*	0	Fixed
Dil. Sloan-g'	$0.55^{+0.16}_{-0.20}$	$\mathcal{U}(-1,1)$
Dil. Sloan-r'	$0.13^{+0.18}_{-0.19}$	$\mathcal{U}(-1,1)$
Dil. *Ic*	$-0.08^{+0.12}_{-0.13}$	$\mathcal{U}(-1,1)$
Dil. I+z	$-0.07^{+0.09}_{-0.10}$	$\mathcal{U}(-1,1)$
Dil. 1.41 μm	-0.00 ± -0.21	$\mathcal{U}(-1,1)$

flexibility of the fit obtained by combining a GP and a free dilution term. We repeated the analysis by using the hybrid spline function of `Allesfitter` instead of the GP to constrain the dilution better while still accounting for the red noise in the data. Unfortunately, the large systematic effects and poor precision in the Sloan-g' band did not allow a good fit of the light curves. Discarding the bluest band, this analysis still spans the range between 550 and 1000 nm with no overlap between the I+z and Sloan-r' filters, and shows no significant chromatic behaviour.

In addition, we made use of the TRICERATOPS[7] package (S. Giacalone et al. 2021) to statistically validate TOI-237 c. It offers a Bayesian framework to evaluate the FPP and NFPP to support the planet hypothesis. It calculates the probability for a collection of astrophysical false positive scenarios from the flux of nearby stars, and a planet is statistically validated if the FPP < 0.015 and an NFPP $< 10^{-3}$. Considering the low S/N of the *TESS* data for TOI-237 c, we performed the analysis on the phase-folded data from TRAPPIST-South which offers a better precision. Given that the star is isolated, no nearby false positive scenarios were considered, and the NFPP is 0.

We observed TOI-237 on 2022 August 1 with the Zorro speckle imager mounted on the Gemini South 8-m telescope (N. J. Scott et al. 2021) as a part of the *TESS* follow-up observing program. Eleven sets of 1000×0.06 s observations were simultaneously obtained in narrow band 562 and 832 nm filters and processed in our standard Fourier analysis software pipeline (S. B. Howell et al. 2011). Fig. C1 shows the result of this high-resolution optical image showing the 5σ magnitude contrast curves obtained from these observations from the telescope diffraction limit out to 1.2 arcsec. TOI-237 is a single star to within the contrast limits obtained (4.5–5.5 mag) over the angular limits of the observation. At the distance of TOI-237 (d= 38 pc), these angular limits correspond to spatial limits of 0.76 to 46 au. We included this sensitivity curve in the TRICERATOPS analysis to reduce the probabilities of scenarios involving an unresolved background star. It yielded an FPP of 0.0011, which classifies TOI-237 c as a statistically validated planet.

6.2 TOI-4336 A c

In the case of TOI-4336 A, L. Parc et al. (2026) present the masses of both planets in the system using data from the ESPRESSO (Echelle SPectrograph for Rocky Exoplanets and Stable Spectroscopic Observations) and NIRPS (Near Infra Red Planet Searcher) spectrographs. This publication coordinated with ours, and their analysis includes priors from our photometric analysis. The masses obtained are of 3.33 ± 0.36 and $1.55 \pm 0.13 M_\oplus$ for TOI-4336 A b and TOI-4336 A c, respectively.

[7] https://github.com/stevengiacalone/triceratops/tree/master

7 DYNAMICAL ANALYSIS

In this section, we seek to determine whether there are any stability limitations for TOI-237 and TOI-4336 A, given the newly discovered planets. With this goal, we used the mean exponential growth factor of nearby orbits, $Y(t)$ (MEGNO; P. Cincotta & C. Simó 1999; P. M. Cincotta & C. Simó 2000; P. M. Cincotta, C. M. Giordano & C. Simó 2003) parameter, a chaos index widely used to explore the stability of planetary systems (see e.g. M. N. Günther et al. 2019; J. Horner et al. 2019; J. S. Jenkins et al. 2019). In particular, we employed the MEGNO implementation with the N-body integrator REBOUND (H. Rein & S. F. Liu 2012), which employs the Wisdom–Holman WHFAST code (H. Rein & D. Tamayo 2015). It is worth noting that, for TOI-4336 A, we did not, for simplicity, consider the other two stars in this hierarchical triple system, which are far enough away to have no influence, as demonstrated in section 6.2 of M. Timmermans et al. (2024).

For each system, we conducted two simulation suites to explore orbital stability as a function of the two unknown planetary parameters that contribute most to stability: eccentricity and planetary mass. We built two-dimensional MEGNO-maps in the M_b–M_c and e_b–e_c parameter spaces following B.-O. Demory et al. (2020). On the one hand, to explore realistic planetary mass ranges, we used the SPRIGHT code (H. Parviainen, R. Luque & E. Palle 2024) and set the lower and upper limits to the 2σ values obtained; that is: $1.3 \leq M_b \leq 3.7\,M_\oplus$ and $1.2 \leq M_b \leq 2.3\,M_\oplus$ for planets TOI-237 b and c, respectively, and $3.0 \leq M_b \leq 13.2\,M_\oplus$ and $1.0 \leq M_b \leq 2.6\,M_\oplus$ for planets TOI-4336 A b and c. On the other hand, we set the minimum and maximum planetary eccentricities to 0.0 and 0.1, motivated by population-level studies which indicate that compact multi-planetary systems tend to have low-eccentricity architectures, with values typically $\lesssim$0.1 (e.g. M. Y. He et al. 2020).

In our analyses, we selected 100 values from each range, yielding 10 000 mutual combinations per simulation. We fixed the other parameters to their nominal values given in Tables 4 and 5. The integration time was set to 1 million orbits of the outermost planet, and the time-step was set to 5 per cent of the orbital period of the innermost planet. We found that, within the parameter range explored, both systems are highly stable, with fewer than 0.01 per cent of scenarios exhibiting unstable configurations, indicating their reliability as dynamically viable planetary architectures. Therefore, the dynamical robustness of the systems reinforces the credibility of the inferred orbital solutions and supports the planetary nature interpretation of the newly detected companions.

As described earlier, the orbital periods of TOI-237 b and c yield a period ratio of $P_b/P_c \approx 3.1155$, which lies only ∼3.85 per cent above the exact 3:1 second-order mean-motion resonance. Although the system is not exactly at the nominal commensurability, its proximity might suggest that resonant or near-resonant interactions remain dynamically relevant. Such a configuration may allow mutual gravitational perturbations to produce measurable TTVs. To explore this scenario, we generated a set of 10 000 synthetic system realizations by varying orbital periods, planetary masses, eccentricities, and orbital angles following F. J. Pozuelos et al. (2023) and S. Zúñiga-Fernández et al. (2025). We found that the maximum TTV amplitude for both planets remains below 1 s, indicating that the system is unlikely to be in,

or even near, a dynamically active resonance. This result further supports the picture of a long-term, stable architecture, in which resonant forcing plays a negligible role in the current dynamical evolution of the system.

8 DISCUSSION AND CONCLUSIONS

The Hidden Gems project aims to find new planets in known transiting systems. Given the high probability of multiple planet systems, especially for rocky planets orbiting low-mass stars, those hosting at least one transiting planet are likely to host more. Our project uses the capabilities of SHERLOCK to identify low S/N signals in the *TESS* data and produce new planet candidates. We validate the planetary nature of two new warm likely super-Earths: TOI-237 c and TOI-4336 A c.

TOI-237 c has a radius of 1.21 ± 0.04 $R_\oplus$ and orbits a mid-M star with a radius of $0.206^{+0.005}_{-0.007}$ $R_\odot$ every 1.74 d. It is a companion to TOI-237 b, the first transiting planet found in the system (W. C. Waalkes et al. 2021). Our re-analysis of all the available ground-based data yields a radius of 1.38 ± 0.04 $R_\oplus$ for planet b orbiting with a period of 5.43 d. This is consistent with the results from W. C. Waalkes et al. (2021), with an uncertainty on the radius reduced by a factor of three. We performed model comparisons and found that the circular case for planets b and c is favoured. Although TOI-237 b and c are near 3:1 mean-motion resonance, our dynamical simulations revealed a highly stable system with TTVs of the order of 1 s, which cannot be detected with the current technology. Similarly, we find TOI-4336 A c, a planet with a radius of 1.17 ± 0.06 $R_\oplus$ orbiting with a period of 7.59 d. It is an inner companion to TOI-4336 A b first published in M. Timmermans et al. (2024). We also find consistent results with a radius of 2.04 ± 0.07 $R_\oplus$ for TOI-4336 A b. The model comparison analysis yielded a slight eccentricity for planet c of $0.09^{+0.16}_{-0.07}$, and a circular orbit for planet b. The dynamical analysis also supports a stable configuration in the case of the TOI-4336 A system.

8.1 In the context of the radius valley

The radius valley is a remarkable bimodal feature in the distribution of small planet radii with periods under 100 d. First discovered for FGK stars, B. J. Fulton et al. (2017) calculated the deficit of planets to occur at ~ 1.7 $R_\oplus$. Planets were then categorized according to their radius, with the smaller ones being likely super-Earths with rocky cores and thin atmospheres, and the larger ones being likely sub-Neptunes with rocky cores and puffy atmospheres. The separation between the two originates from mass-loss processes such as photoevaporation (H. Chen & L. A. Rogers 2016; J. E. Owen & Y. Wu 2017) and core-powered mass loss (A. Gupta & H. E. Schlichting 2019). Further investigation into the radius valley for low-mass stars gave conflicting results, with some papers supporting its existence or fading (e.g. R. Cloutier & K. Menou 2020; V. Van Eylen et al. 2021; A. Bonfanti et al. 2024; H. M. Parashivamurthy & G. D. Mulders 2025), while others argued for a density valley (R. Luque & E. Pallé 2022) or a continuous distribution of core compositions and atmospheres (L. Parc et al. 2024). Fig. 7 shows the location of the planets from both systems with respect to the radius valley limits calculated in R. Cloutier & K. Menou (2020), for M dwarfs in the radius–period parameter space. The TOI-237 planets lie below the limit in the likely super-Earths category. The TOI-4336 A system holds one planet on either side of the gap, making it an ideal case to study atmospheric loss processes in a low-mass star environment.

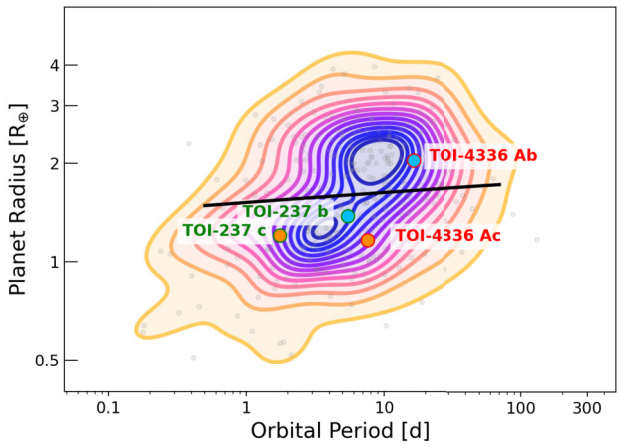

Figure 7. Planet radius versus orbital period for transiting planets with radii $R_p < 4R_\oplus$ orbiting low-mass stars with $T_{eff} < 4000$ K. Contours are kernel density estimates which highlight the density of these points. The radius valley is apparent from the bimodal distribution of the data. We illustrate its position with solid black lines, which are taken from R. Cloutier & K. Menou (2020). The planets of the TOI-237 system are labelled in green, the ones of the TOI-4336 A system in red, with planets b marked as blue points and, planets c marked as orange points.

8.2 Prospects for atmospheric characterization

With the SPRIGHT package (H. Parviainen et al. 2024), based on a probabilistic mass-radius relation for small planets, we obtained theoretical masses of $2.77^{+0.43}_{-0.47}$ and $1.73^{+0.27}_{-0.23}$ $M_\oplus$ for planets b and c of the TOI-237 system, respectively. For the TOI-4336 A system, we obtain masses of $5.82^{+1.88}_{-1.32}$ and $1.53^{+0.37}_{-0.33}$ $M_\oplus$. We can evaluate the potential of these planets for atmospheric studies by their transmission and emission spectroscopy metrics (TSM and ESM) as described in E. M.-R. Kempton et al. (2018), this is illustrated in Fig. 8. These metrics provide a framework to prioritize atmospheric investigation of planets. They are based on the expected S/N with the *James Webb Space Telescope* (*JWST*)/NIRISS (Near Infrared Imager and Slitless Spectrograph) instrument for a synthetic population. TOI-237 b, c, and TOI-4336 A c lie in the terrestrial regime with $R_p < 1.5R_\oplus$, with TSM values of 7, 11, and 10, respectively. TOI-237 c and TOI-4336 A c are good candidates for transmission spectroscopy as they are close to the recommended threshold of 10. Similarly, TOI-4336 A b is in the small sub-Neptune regime with $R_p < 2.75R_\oplus$, and has a TSM value of 71. While the recommended threshold is 90, this planet has already proven to be of high interest for atmospheric exploration with observations from *HST* (P16875) and *JWST* Cycle 3 (P4711). TOI-237 c is also a good candidate for emission photometry with *JWST*, with an ESM of 2. This value is larger than TRAPPIST-1 c (ESM of 1.4), where a thick atmosphere was ruled out by a phase curve obtained with *JWST*/MIRI (M. Gillon et al. 2025).

Given their small sizes, we can estimate the likelihood of TOI-237 b, c and TOI-4336 A c of having retained their atmosphere along the lifetime of the systems. The theoretical limit between planets having retained an atmosphere and the ones having lost it by hydrodynamic escape due to stellar X-ray and ultraviolet (XUV) flux is called the 'cosmic shoreline' (K. J. Zahnle & D. C. Catling 2017). This has motivated the recent *JWST* Rocky

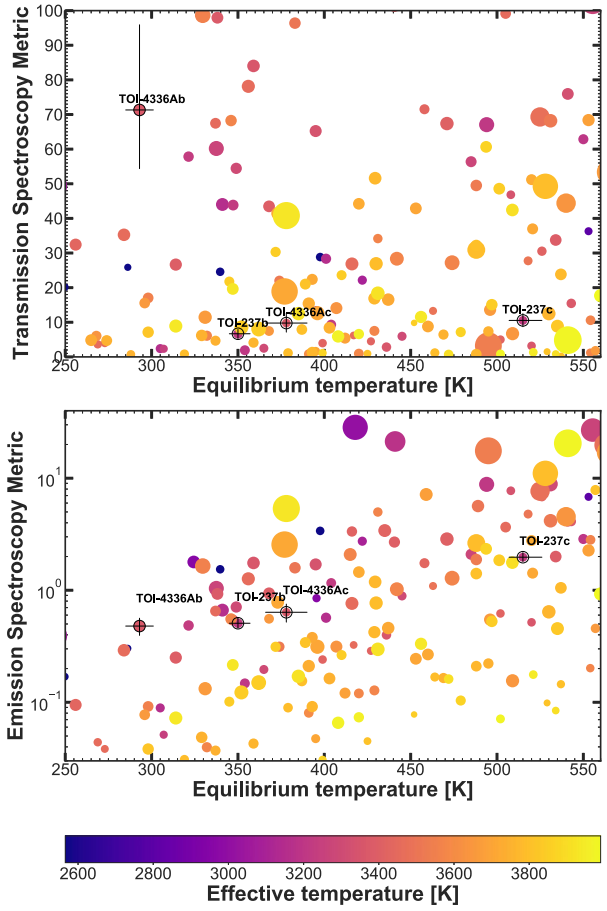

Figure 8. Both panels represent the population of known transiting exoplanets with mass measurements, the colour bar shows the effective temperatures of the host stars and the size of the data points are proportional to the radii of the planets. The top and bottom panels show the TSM and ESM versus the equilibrium temperature of the planets. The planets presented in this paper are highlighted with black circles and error bars.

Worlds Director's Discretionary Time programme[8] (S. Redfield et al. 2024) to search for atmospheres around rocky exoplanets. In that context, E. K. Pass, D. Charbonneau & A. Vanderburg (2025) estimated the cosmic shoreline for mid-to-late M dwarfs, and computed the cumulative historic XUV irradiation of TOI-237 b, as given in their table 2. They find $I_{\rm XUV} = 230\, I_{\rm XUV,\oplus}$ and an escape velocity of $v_{\rm esc} = 18.2\,{\rm km\,s^{-1}}$), corresponding to an atmosphere retention metric of ARM $= -0.63$, where a negative value indicates the planet most likely has not retained its atmosphere. We perform a similar calculation for TOI-237 c and TOI-4336 A c, and find $I_{\rm XUV} = 1133\, I_{\rm XUV,\oplus}$ and $108\, I_{\rm XUV,\oplus}$,[9] respectively, yielding ARM values of -1.70 and -0.76, thus it is unlikely that these planets would retain a primary atmosphere.

[8] https://rockyworlds.stsci.edu/

[9] Based on the table 1 coefficients of E. K. Pass et al. (2025) for a star with $M = 0.20\,{\rm M}_\odot$ for TOI-237, and $M = 0.30\,{\rm M}_\odot$ for TOI-4336 A.

8.3 Prospects for mass measurements

Finally, W. C. Waalkes et al. (2021) estimated that given the faintness of TOI-237 and an estimated RV semi-amplitude of 3.4 ms^{-1}, a mass measurements for TOI-237 b would be very difficult for CARMENES (Calar Alto high-Resolution search for M dwarfs with Exoearths with Near-infrared and optical Echelle Spectrographs; A. Quirrenbach et al. 2010), the Habitable Zone Planet Finder (S. Mahadevan et al. 2012), as well as the IRD instrument (InfraRed Doppler; T. Kotani et al. 2014) on the *Subaru* telescope. We consider here the ESPRESSO spectrograph on the Very Large Telescope (T. Kotani et al. 2014) and the NIRPS spectrograph (F. Bouchy et al. 2017), which are both well-suited to observe small planets orbiting low-mass stars. We find an RV semi-amplitude of 3.30 ms^{-1} for the theoretical masses mentioned previously. We find that ESPRESSO and NIRPS would have precisions of the order of 8.04 and 12.45 ms^{-1}, respectively, using the ESPRESSO ETC and the NIRPS precision estimates from the H magnitude. This corresponds to 53 and 128 measurements for a 3σ detection for each of those instruments. For TOI-237 c, the RV semi-amplitude would be 3.01 ms^{-1}, which corresponds to 64 and 154 measurements respectively for ESPRESSO and NIRPS. Overall, it seems unlikely a mass measurement could be obtained from the ground for the TOI-237 planets considering the amount of telescope time it would require. In the case of the TOI-4336 A system, a high-significance detection of the RV semi-amplitudes was obtained with the NIRPS spectrograph, and we refer to (L. Parc et al. 2026) for the mass measurements.

ACKNOWLEDGEMENTS

For the purpose of open access, the author has applied a Creative Commons Attribution (CC BY) licence to the Author Accepted Manuscript version arising from this submission.

This work makes use of observations from the LCOGT network. Part of the LCOGT telescope time was granted by NOIRLab through the Mid-Scale Innovations Program (MSIP). MSIP is funded by NSF.

This is paper is based on observations made with the MuSCAT3 instrument, developed by the Astrobiology Center and under financial supports by JSPS KAKENHI (JP18H05439) and JST PRESTO (JPMJPR1775), at Faulkes Telescope North on Maui, HI, operated by the Las Cumbres Observatory.

This research has made use of the Exoplanet Follow-up Observation Program (ExoFOP; doi:10.26134/ExoFOP5) website, which is operated by the California Institute of Technology, under contract with the National Aeronautics and Space Administration under the Exoplanet Exploration Program.

Funding for the *TESS* mission is provided by NASA's Science Mission Directorate. KAC acknowledges support from the *TESS* mission via subaward s3449 from MIT.

The ULiege's contribution to SPECULOOS has received funding from the European Research Council under the European Union's Seventh Framework Programme (FP/2007-2013) (grant agreement no. 336480/SPECULOOS), from the Balzan Prize and Francqui Foundations, from the Belgian Scientific Research Foundation (F.R.S.-FNRS; grant no. T.0109.20), from the University of Liege, and from the ARC grant for Concerted Research Actions financed by the Wallonia-Brussels Federation. The Cambridge contribution and work are supported by a grant from the Simons Foundation (PI: Queloz, grant no. 327127). The Birmingham contribution to SPECULOOS has received fund

from the European Research Council (ERC) under the European Union's Horizon 2020 research and innovation programme (grant agreement no. 803193/BEBOP), from the MERAC foundation, from the Science and Technology Facilities Council (STFC; grants nos ST/S00193X/1, ST/W000385/1, and ST/Y001710/1) and from the ERC/UKRI Frontier Research Guarantee programme (EP/Z000327/1/CandY).

TRAPPIST is funded by the Belgian Fund for Scientific Research (Fond National de la Recherche Scientifique, FNRS) under the grant PDR T.0120.21. MG and EJ are F.R.S.-FNRS Research Directors. Data were collected at the ESO Silla Observatory. YGMC is partially supported by UNAM PAPIIT-IG101224 and the Swiss National Science Foundation IZSTZ0_216537.

This publication benefits from the support of the French Community of Belgium in the context of the FRIA Doctoral Grant awarded to MT. FJP acknowledges financial support from the Severo Ochoa grant CEX2021-001131-S funded by MCIN/AEI/10.13039/501100011033 and Ministerio de Ciencia e Innovación through the project PID2022-137241NB-C43. BR-A acknowledges funding support from ANID Basal project FB210003. MG is F.R.S-FNRS Research Director. Funding for KB was provided by the European Union (ERC AdG SUBSTELLAR, GA 101054354). This work is partly supported by JSPS KAKENHI grant nos JP24H00017, JP24K00689, and JSPS Bilateral Program no. JPJSBP120249910. This material is based upon work supported by the National Aeronautics and Space Administration under agreement no. 80NSSC21K0593 for the program 'Alien Earths'. The results reported herein benefited from collaborations and/or information exchange within NASA's Nexus for Exoplanet System Science (NExSS) research coordination network sponsored by NASA's Science Mission Directorate. This material is based upon work supported by the European Research Council (ERC) Synergy Grant under the European Union's Horizon 2020 research and innovation program (grant no. 101118581 – project REVEAL).

DATA AVAILABILITY

TESS data products are available via the MAST portal at https://mast.stsci.edu/portal/Mashup/Clients/Mast/Portal.html. Follow-up observations (photometry, high-resolution imaging data) are available on ExoFOP or on request.

REFERENCES

Allard F., Homeier D., Freytag B., 2012, Phil. Trans. R. Soc. Lond. Ser. A, 370, 2765
Allard F., Homeier D., Freytag B., 2013, Mem. Soc. Astron. Ital. Suppl., 24, 128
Asplund M., Grevesse N., Sauval A. J., Scott P., 2009, ARA&A, 47, 481
Bonfanti A. et al., 2024, A&A, 682, A66
Bonfils X. et al., 2015, in Shaklan S., ed., Proc. SPIE Conv. Ser. Vol. 9605, Techniques and Instrumentation for Detection of Exoplanets VII. SPIE, Bellingham, p. 96051L
Borucki W. J. et al., 2010, Science, 327, 977
Bouchy F. et al., 2017, The Messenger, 169, 21
Brown T. M. et al., 2013, PASP, 125, 1031
Buchner J., 2021, J. Open Source Softw., 6, 3001
Caffau E., Ludwig H.-G., Steffen M., Freytag B., Bonifacio P., 2011, Sol. Phys., 268, 255
Carrasco J. M. et al., 2021, A&A, 652, A86
Chen H., Rogers L. A., 2016, ApJ, 831, 180
Cincotta P., Simó C., 1999, Celest. Mech. Dynam. Astron., 73, 195
Cincotta P. M., Simó C., 2000, A&AS, 147, 205
Cincotta P. M., Giordano C. M., Simó C., 2003, Phys. D: Nonlinear Phenom., 182, 151
Claret A., 2018, A&A, 618, A20
Claret A., Hauschildt P. H., Witte S., 2012, A&A, 546, A14
Clemens J. C., Crain J. A., Anderson R., 2004, in Moorwood A. F. M., Iye M., eds, Proc. SPIE Conf. Ser., Vol. 5492, Ground-based Instrumentation for Astronomy. SPIE, Bellingham, p. 331
Cloutier R., Menou K., 2020, AJ, 159, 211
Cutri R. M. et al., 2003, VizieR Online Data Catalog: 2MASS All-Sky Catalog of Point Sources (Cutri+ 2003). preprint (VizieR On-line Data Catalog: II/246. Originally published in: 2003yCat.2246....0C)
Cutri R. M. et al., 2021, VizieR Online Data Catalog: AllWISE Data Release (Cutri+ 2013). preprint (VizieR On-line Data Catalog: II/328. Originally published in: IPAC/Caltech (2013))
De Angeli F. et al., 2023, A&A, 674, A2
Delrez L. et al., 2018, in Marshall H. K., Spyromilio J., eds, Proc. SPIE Conf. Ser. Vol. 10700, Ground-based and Airborne Telescopes VII. SPIE, Bellingham, p. 107001I
Delrez L. et al., 2022, A&A, 667, A59
Demory B.-O. et al., 2020, A&A, 642, A49
Dévora-Pajares M., Pozuelos F. J, Thuillier A., Timmermans M., Van Grootel V., Bonidie V., Mota L. C., Suárez J. C, 2024. MNRAS, 532, 4752
Dévora-Pajares M., Pozuelos F. J., Suárez J. C., González-Penedo M., Dafonte C., 2025, preprint (arXiv:2511.08768)
Dransfield G. et al., 2024, MNRAS, 527, 35
Dressing C. D., Charbonneau D., 2013, ApJ, 767, 95
Foreman-Mackey D., 2018, Res. Notes Am. Astron. Soc., 2, 31
Foreman-Mackey D., Agol E., Ambikasaran S., Angus R., 2017, Astrophysics Source Code Library, record ascl:1709.008
Fulton B. J. et al., 2017, AJ, 154, 109
Gaia Collaboration, 2023, A&A, 674, A1
Garcia L. J., Timmermans M., Pozuelos F. J., Ducrot E., Gillon M., Delrez L., Wells R. D., Jehin E., 2021, Astrophysics Source Code Library, record ascl:2111.006
Garcia L. J., Timmermans M., Pozuelos F. J., Ducrot E., Gillon M., Delrez L., Wells R. D., Jehin E., 2022, MNRAS, 509, 4817
Giacalone S. et al., 2021, AJ, 161, 24
Gillon M., Jehin E., Magain P., Chantry V., Hutsemékers D., Manfroid J., Queloz D., Udry S., 2011a, EPJ Web Conf., 11, 06002
Gillon M., Bonfils X., Demory B.-O., Seager S., Deming D., Triaud A. H. M. J., 2011b, A&A, 525, A32
Gillon M. et al., 2025, preprint (arXiv:2509.02128)
Gizis J. E., Reid I. N., 1997, PASP, 109, 849
Guerrero N. M. et al., 2021, ApJS, 254, 39
Günther M. N., Daylan T., 2019, Astrophysics Source Code Library, record ascl:1903.003
Günther M. N., Daylan T., 2021, ApJS, 254, 13
Günther M. N. et al., 2019, Nat. Astron., 3, 1099
Gupta A., Schlichting H. E., 2019, MNRAS, 487, 24
He M. Y., Ford E. B., Ragozzine D., Carrera D., 2020, AJ, 160, 276
Hippke M., Heller R., 2019, A&A, 623, A39
Hippke M., David T. J., Mulders G. D., Heller R., 2019, AJ, 158, 143
Horner J. et al., 2019, AJ, 158, 100
Howell S. B., Everett M. E., Sherry W., Horch E., Ciardi D. R., 2011, AJ, 142, 19
Howell S. B. et al., 2014, PASP, 126, 398
Hsu D. C., Ford E. B., Terrien R., 2020, MNRAS, 498, 2249
Husser T.-O., Wende-von Berg S., Dreizler S., Homeier D., Reiners A., Barman T., Hauschildt P. H., 2013, A&A, 553, A6
Iyer A. R. et al., 2023, ApJ, 944, 41
Jehin E. et al., 2011, The Messenger, 145, 2
Jenkins J. M. et al., 2016, in Chiozzi G., Guzman J. C., eds, Proc. SPIE Conf. Ser. Vol. 9913, Software and Cyberinfrastructure for Astronomy IV. SPIE, Bellingham, p. 99133E
Jenkins J. S., Pozuelos F. J., Tuomi M., Berdiñas Z. M., Díaz M. R., Vines J. I., Suárez J. C., Peña Rojas P. A., 2019, MNRAS, 490, 5585

Jensen E., 2013, Astrophysics Source Code Library, record ascl:1306.007
Kass R. E., Raftery A. E., 1995, J. Am. Stat. Assoc., 90, 773
Kempton E. M.-R. et al., 2018, PASP, 130, 114401
Kesseli A. Y., West A. A., Veyette M., Harrison B., Feldman D., Bochanski J. J., 2017, ApJS, 230, 16
Kipping D. M., 2013, MNRAS, 435, 2152
Kotani T. et al., 2014, in Ramsay S. K., McLean I. S., Takami H., eds, Proc. SPIE Conf. Ser. Vol. 9147, Ground-based and Airborne Instrumentation for Astronomy V. SPIE, Bellingham, p. 914714
Lépine S., Rich R. M., Shara M. M., 2003, AJ, 125, 1598
Lépine S., Rich R. M., Shara M. M., 2007, ApJ, 669, 1235
Lépine S., Hilton E. J., Mann A. W., Wilde M., Rojas-Ayala B., Cruz K. L., Gaidos E., 2013, AJ, 145, 102
Lightkurve Collaboration, 2018, Astrophysics Source Code Library, record ascl:1812.013
Luque R., Pallé E., 2022, Science, 377, 1211
Mahadevan S. et al., 2012, in McLean I. S., Ramsay S. K., Takami H., eds, Proc. SPIE Conf. Ser. Vol. 8446, Ground-based and Airborne Instrumentation for Astronomy IV. SPIE, Bellingham, p. 84461S
Mann A. W., Brewer J. M., Gaidos E., Lépine S., Hilton E. J., 2013, AJ, 145, 52
Mann A. W., Feiden G. A., Gaidos E., Boyajian T., von Braun K., 2015, ApJ, 804, 64
Mann A. W. et al., 2019, ApJ, 871, 63
Maxted P. F. L., 2016, A&A, 591, A111
McCully C., Volgenau N. H., Harbeck D.-R., Lister T. A., Saunders E. S., Turner M. L., Siiverd R. J., Bowman M., 2018, in Guzman J. C., Ibsen J., eds, Proc. SPIE Conf. Ser., Vol. 10707, Software and Cyberinfrastructure for Astronomy V. SPIE, Bellingham, p. 107070K
Montegriffo P. et al., 2023, A&A, 674, A3
Muirhead P. S. et al., 2015, ApJ, 801, 18
Mulders G. D., Pascucci I., Apai D., 2015, ApJ, 798, 112
Narita N. et al., 2020, in Evans C. J., Bryant J. J., Motohara K., eds, Proc. SPIE Conf. Ser. Vol. 11447, Ground-based and Airborne Instrumentation for Astronomy VIII. SPIE, Bellingham, p. 114475K
Owen J. E., Wu Y., 2017, ApJ, 847, 29
Parashivamurthy H. M., Mulders G. D., 2025, A&A, 703, A8
Parc L., Bouchy F., Venturini J., Dorn C., Helled R., 2024, A&A, 688, A59
Parc L. et al., 2026, A&A, 781, A81
Parviainen H., Aigrain S., 2015, MNRAS, 453, 3821
Parviainen H., Luque R., Palle E., 2024, MNRAS, 527, 5693
Pass E. K., Charbonneau D., Vanderburg A., 2025, ApJ, 986, L3
Pecaut M. J., Mamajek E. E., 2013, ApJS, 208, 9
Pedersen P. P. et al., 2024, in Bryant J. J., Motohara K., Vernet J. R. D., eds, Proc. SPIE Conf. Ser., Vol. 13096, Ground-based and Airborne Instrumentation for Astronomy X. SPIE, Bellingham, p. 130963X
Pozuelos F. J. et al., 2020, A&A, 641, A23
Pozuelos F. J. et al., 2023, A&A, 672, A70
Prochaska J. et al., 2020, J. Open Source Softw., 5, 2308
Prochaska J. X. et al., 2020, pypeit/PypeIt: Release 1.0.0, Zenodo
Quirrenbach A. et al., 2010, in McLean I. S., Ramsay S. K., Takami H., eds, Proc. SPIE Conf. Ser., Vol. 7735, Ground-based and Airborne Instrumentation for Astronomy III. SPIE, Bellingham, p. 773513
Rasmussen C. E., Williams C. K. I., 2006, Gaussian Processes for Machine Learning
Redfield S. et al., 2024, preprint (arXiv:2404.02932)
Reid I. N., Hawley S. L., Gizis J. E., 1995, AJ, 110, 1838
Rein H., Liu S. F., 2012, A&A, 537, A128
Rein H., Tamayo D., 2015, MNRAS, 452, 376
Ricker G. R. et al., 2015, J. Astron. Telesc. Instrum. Syst., 1, 014003
Riddick F. C., Roche P. F., Lucas P. W., 2007, MNRAS, 381, 1067
Savitzky A., Golay M. J. E., 1964, Anal. Chem., 36, 1627
Scott N. J. et al., 2021, Front. Astron. Space Sci., 8, 138
Sebastian D. et al., 2021, A&A, 645, A100
Speagle J. S., 2020, MNRAS, 493, 3132
Stolker T. et al., 2020, A&A, 635, A182
Timmermans M. et al., 2024, A&A, 687, A48
Van Eylen V. et al., 2021, MNRAS, 507, 2154
Vines J. I., Jenkins J. S., 2022, MNRAS, 513, 2719
Waalkes W. C. et al., 2021, AJ, 161, 13
West A. A., Hawley S. L., Bochanski J. J., Covey K. R., Reid I. N., Dhital S., Hilton E. J., Masuda M., 2008, AJ, 135, 785
Zahnle K. J., Catling D. C., 2017, ApJ, 843, 122
Zúñiga-Fernández S. et al., 2025, A&A, 702, A85

APPENDIX A: PRIOR AND POSTERIOR DISTRIBUTIONS OF THE LIMB-DARKENING COEFFICIENTS USED IN THE GLOBAL ANALYSES OF THE PHOTOMETRY.

Table A1. Limb-darkening coefficients obtained in the global analysis of the TOI-237 system (see Section 5).

Parameters	Values	Priors	Source
Limb-darkening $q_{1,\mathrm{TESS}}$	$0.399^{+0.045}_{-0.043}$	$\mathcal{N}(0.398, 0.050^2)$	Fitted
Limb-darkening $q_{2,\mathrm{TESS}}$	$0.123^{+0.046}_{-0.045}$	$\mathcal{N}(0.121, 0.050^2)$	Fitted
Limb-darkening $q_{1,I+z}$	$0.293^{+0.040}_{-0.043}$	$\mathcal{N}(0.316, 0.050^2)$	Fitted
Limb-darkening $q_{2,I+z}$	$0.170^{+0.042}_{-0.043}$	$\mathcal{N}(0.184, 0.050^2)$	Fitted
Limb-darkening $q_{1,\mathrm{Sloan}-g'}$	$0.678^{+0.046}_{-0.045}$	$\mathcal{N}(0.686, 0.050^2)$	Fitted
Limb-darkening $q_{2,\mathrm{Sloan}-g'}$	0.285 ± 0.044	$\mathcal{N}(0.289, 0.050^2)$	Fitted
Limb-darkening $q_{1,Ic}$	0.373 ± 0.044	$\mathcal{N}(0.376, 0.050^2)$	Fitted
Limb-darkening $q_{2,Ic}$	0.171 ± 0.045	$\mathcal{N}(0.173, 0.050^2)$	Fitted
Limb-darkening $q_{1,\mathrm{ExTrA}}$	$0.132^{+0.041}_{-0.042}$	$\mathcal{N}(0.121, 0.050^2)$	Fitted
Limb-darkening $q_{2,\mathrm{ExTrA}}$	0.270 ± 0.045	$\mathcal{N}(0.278, 0.050^2)$	Fitted
Limb-darkening $q_{1,\mathrm{Sloan}-r'}$	0.669 ± 0.044	$\mathcal{N}(0.670, 0.050^2)$	Fitted
Limb-darkening $q_{2,\mathrm{Sloan}-r'}$	$0.329^{+0.047}_{-0.046}$	$\mathcal{N}(0.324, 0.050^2)$	Fitted
Limb-darkening $u_{1,\mathrm{TESS}}$	$0.154^{+0.059}_{-0.056}$	–	Derived
Limb-darkening $u_{2,\mathrm{TESS}}$	$0.474^{+0.064}_{-0.065}$	–	Derived
Limb-darkening $u_{1,I+z}$	$0.182^{+0.046}_{-0.047}$	–	Derived
Limb-darkening $u_{2,I+z}$	$0.356^{+0.059}_{-0.055}$	–	Derived
Limb-darkening $u_{1,\mathrm{Sloan}-g'}$	0.469 ± 0.076	–	Derived
Limb-darkening $u_{2,\mathrm{Sloan}-g'}$	0.354 ± 0.074	–	Derived
Limb-darkening $u_{1,Ic}$	$0.207^{+0.058}_{-0.056}$	–	Derived
Limb-darkening $u_{2,Ic}$	$0.400^{+0.061}_{-0.060}$	–	Derived
Limb-darkening $u_{1,\mathrm{ExTrA}}$	0.191 ± 0.047	–	Derived
Limb-darkening $u_{2,\mathrm{ExTrA}}$	$0.163^{+0.045}_{-0.043}$	–	Derived
Limb-darkening $u_{1,\mathrm{Sloan}-r'}$	$0.538^{+0.078}_{-0.079}$	–	Derived
Limb-darkening $u_{2,\mathrm{Sloan}-r'}$	0.280 ± 0.077	–	Derived

Table A2. Limb-darkening coefficients obtained in the global analysis of the TOI-4336 A system (see Section 5).

Parameters	Values	Priors	Source
Limb-darkening $q_{1,\mathrm{TESS}}$	$0.384^{+0.037}_{-0.035}$	$\mathcal{N}(0.376, 0.050^2)$	Fitted
Limb-darkening $q_{2,\mathrm{TESS}}$	$0.106^{+0.034}_{-0.036}$	$\mathcal{N}(0.125, 0.050^2)$	Fitted
Limb-darkening $q_{1,\mathrm{Sloan}-z'}$	$0.291^{+0.032}_{-0.031}$	$\mathcal{N}(0.282, 0.050^2)$	Fitted
Limb-darkening $q_{2,\mathrm{Sloan}-z'}$	$0.136^{+0.024}_{-0.028}$	$\mathcal{N}(0.153, 0.050^2)$	Fitted
Limb-darkening $q_{1,\mathrm{Sloan}-g'}$	$0.647^{+0.032}_{-0.034}$	$\mathcal{N}(0.686, 0.050^2)$	Fitted
Limb-darkening $q_{2,\mathrm{Sloan}-g'}$	$0.293^{+0.037}_{-0.038}$	$\mathcal{N}(0.289, 0.050^2)$	Fitted
Limb-darkening $q_{1,zs}$	0.235 ± 0.036	$\mathcal{N}(0.247, 0.050^2)$	Fitted
Limb-darkening $q_{2,zs}$	$0.282^{+0.037}_{-0.036}$	$\mathcal{N}(0.278, 0.050^2)$	Fitted
Limb-darkening $q_{1,\mathrm{ExTrA}}$	$0.142^{+0.034}_{-0.027}$	$\mathcal{N}(0.110, 0.050^2)$	Fitted
Limb-darkening $q_{2,\mathrm{ExTrA}}$	$0.242^{+0.030}_{-0.035}$	$\mathcal{N}(0.280, 0.050^2)$	Fitted
Limb-darkening $q_{1,\mathrm{Sloan}-r'}$	$0.682^{+0.036}_{-0.037}$	$\mathcal{N}(0.687, 0.050^2)$	Fitted
Limb-darkening $q_{2,\mathrm{Sloan}-r'}$	$0.669^{+0.029}_{-0.032}$	$\mathcal{N}(0.332, 0.050^2)$	Fitted
Limb-darkening $q_{1,\mathrm{Sloan}-i'}$	$0.397^{+0.035}_{-0.037}$	$\mathcal{N}(0.403, 0.050^2)$	Fitted
Limb-darkening $q_{2,\mathrm{Sloan}-i'}$	$0.154^{+0.024}_{-0.031}$	$\mathcal{N}(0.206, 0.050^2)$	Fitted
Limb-darkening $u_{1,\mathrm{TESS}}$	$0.131^{+0.043}_{-0.045}$	–	Derived
Limb-darkening $u_{2,\mathrm{TESS}}$	$0.488^{+0.052}_{-0.050}$	–	Derived
Limb-darkening $u_{1,\mathrm{Sloan}-z'}$	$0.146^{+0.027}_{-0.030}$	–	Derived
Limb-darkening $u_{2,\mathrm{Sloan}-z'}$	$0.392^{+0.040}_{-0.036}$	–	Derived
Limb-darkening $u_{1,\mathrm{Sloan}-g'}$	$0.471\pm^{+0.060}_{-0.059}$	–	Derived
Limb-darkening $u_{2,\mathrm{Sloan}-g'}$	$0.331^{+0.062}_{-0.061}$	–	Derived
Limb-darkening $u_{1,zs}$	$0.271^{+0.041}_{-0.039}$	–	Derived
Limb-darkening $u_{2,zs}$	$0.210^{+0.041}_{-0.039}$	–	Derived
Limb-darkening $u_{1,\mathrm{ExTrA}}$	$0.181^{+0.031}_{-0.030}$	–	Derived
Limb-darkening $u_{2,ExTrA}$	$0.195^{+0.037}_{-0.031}$	–	Derived
Limb-darkening $u_{1,\mathrm{Sloan}-r'}$	$0.528^{+0.056}_{-0.060}$	–	Derived
Limb-darkening $u_{2,\mathrm{Sloan}-r'}$	$0.297^{+0.052}_{-0.047}$	–	Derived

APPENDIX B: TRANSIT MODEL FITS

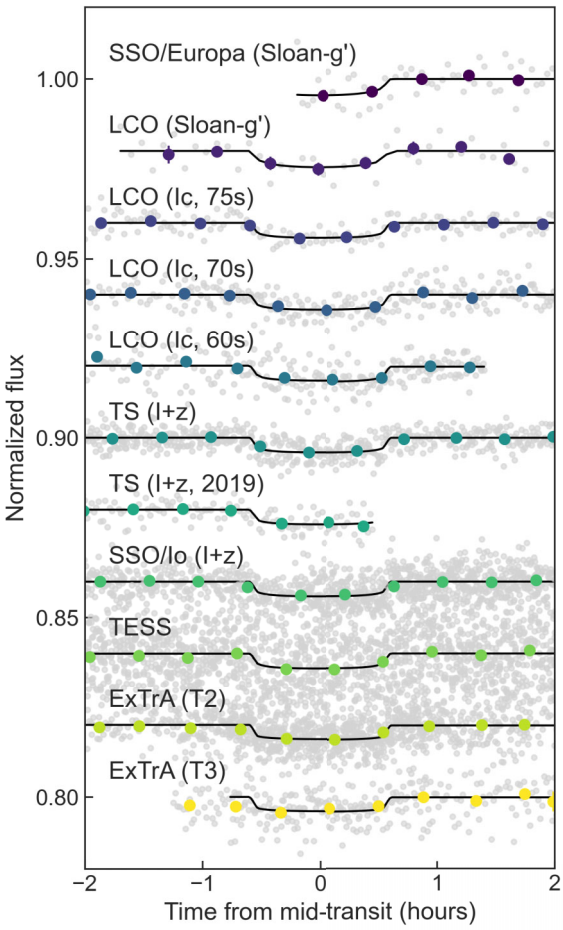

Figure B1. Phase-folded transits of TOI-237 b for each ground-based datasets, they are offset vertically for clarity. The data shown are detrended.

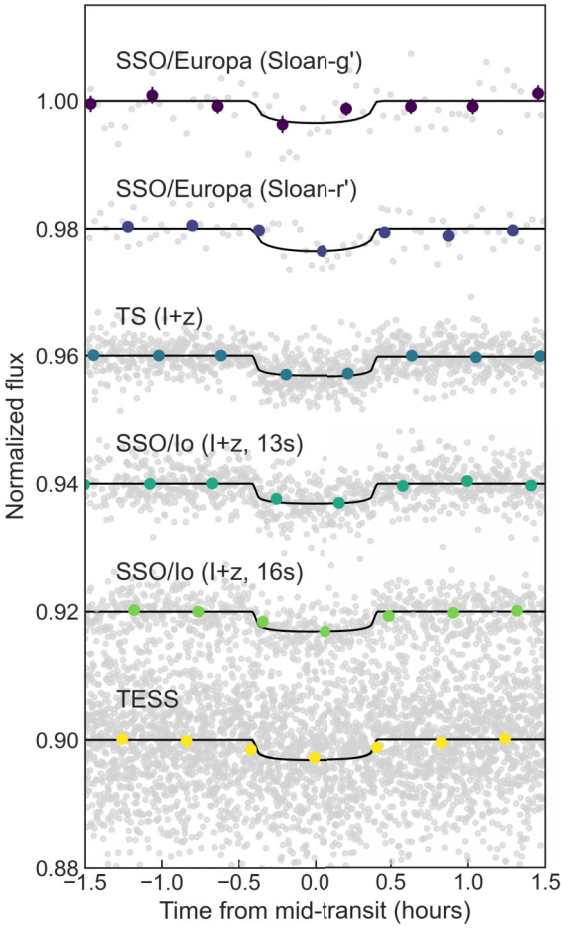

Figure B2. Phase-folded transits of TOI-237 c for each ground-based datasets, they are offset vertically for clarity. The data shown are detrended.

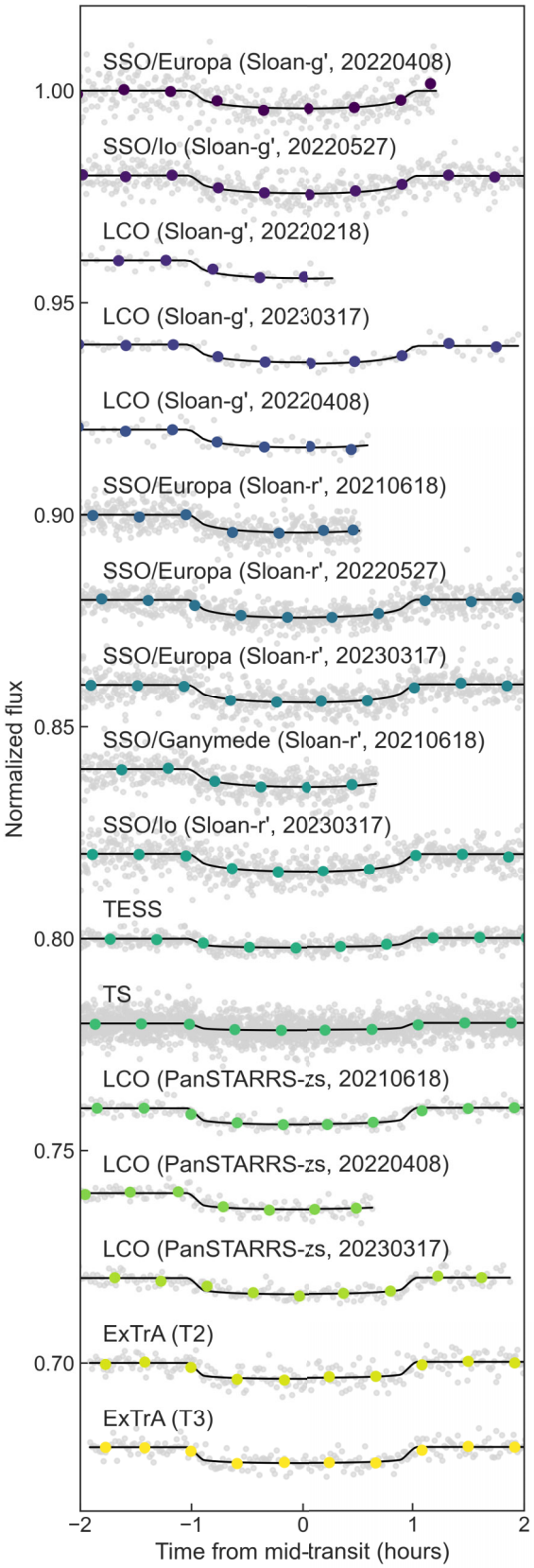

Figure B3. Phase-folded transits of TOI-4336 A bfor each ground-based datasets, they are offset vertically for clarity. The data shown are detrended.

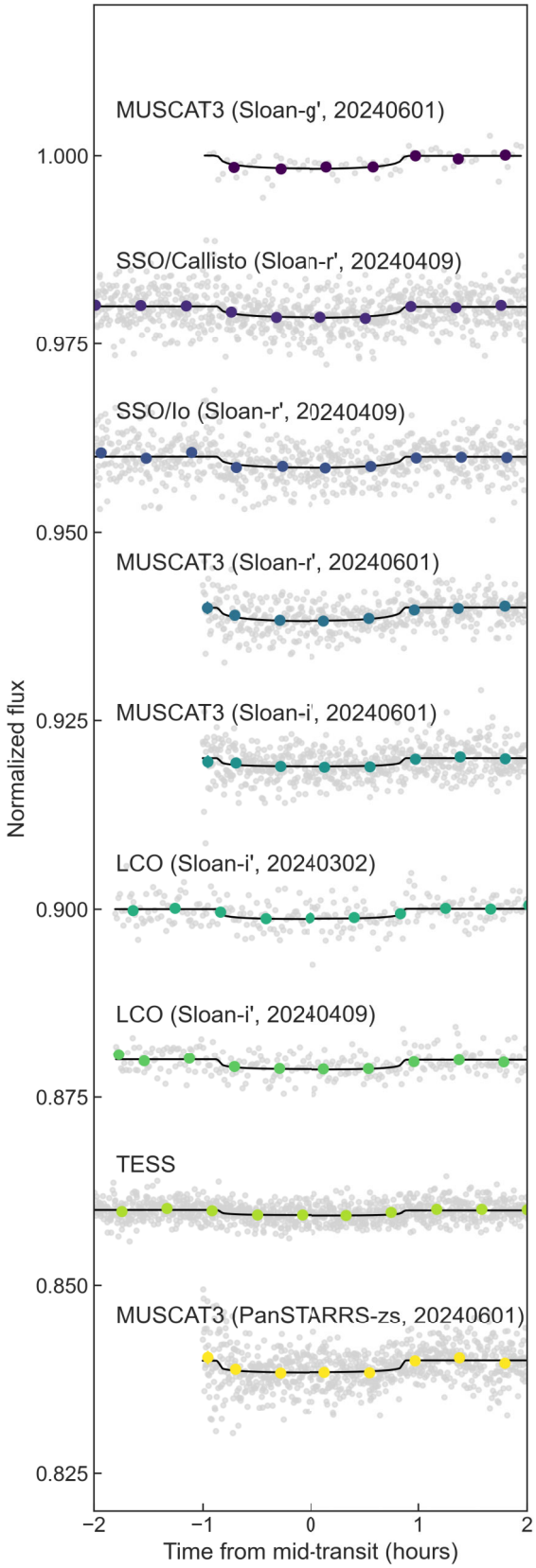

Figure B4. Phase-folded transits of TOI-4336 A c for each ground-based datasets, they are offset vertically for clarity. The data shown is detrended.

APPENDIX C: SPECKLE CONTRAST CURVE

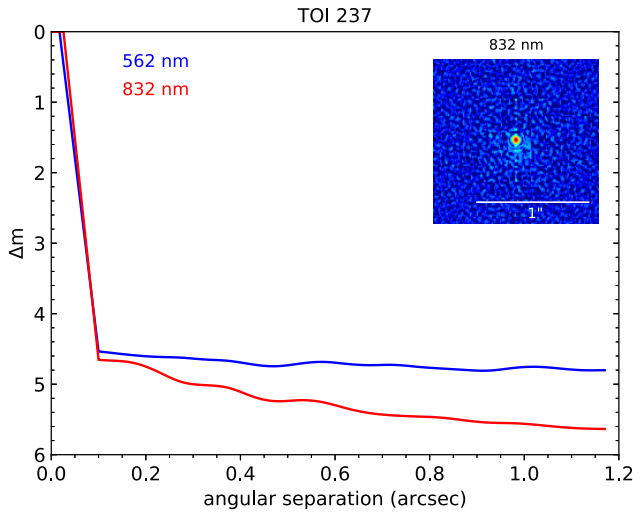

Figure C1. The figure shows 5σ magnitude contrast curves in both filters (562 and 832 nm) as a function of the angular separation out to 1.2 arcsec. The inset shows the reconstructed 832 nm image of TOI-237 with a 1 arcsec scale bar. TOI-237 was found to have no close companions from the diffraction limit (0.02 arcsec) out to 1.2 arcsec to within the contrast levels achieved.

[1]*School of Physics & Astronomy, University of Birmingham, Edgbaston, Birmingham B15 2TT, UK*
[2]*Astrobiology Research Unit, Université de Liège, 19C Allée du 6 Août, B-4000 Liège, Belgium*
[3]*Departamento de Física Teórica y del Cosmos, Universidad de Granada, E-18071 Granada, Spain*
[4]*AI Engineering, Avature, Spain*
[5]*Instituto de Astrofísica de Andalucía (IAA-CSIC), Glorieta de la Astronomía s/n, E-18008 Granada, Spain*
[6]*Instituto de Astrofísica de Canarias (IAC), E-38205 La Laguna, Tenerife, Spain*
[7]*Department of Earth, Atmospheric and Planetary Science, Massachusetts Institute of Technology, 77 Massachusetts Avenue, Cambridge, MA 02139, USA*
[8]*Instituto de Alta Investigación, Universidad de Tarapacá, Casilla 7D, Arica, Chile*
[9]*Observatoire de Genève, Département d'Astronomie, Université de Genève, Chemin Pegasi 51b, CH-1290 Versoix, Switzerland*
[10]*Université Grenoble Alpes, CNRS, IPAG, F-38000 Grenoble, France*
[11]*NASA Ames Research Center, Moffett Field, CA 94035, USA*
[12]*Department of Astronomy & Astrophysics, UC San Diego, 9500 Gilman Drive, La Jolla, CA 92093, USA*
[13]*Center for Astrophysics, Harvard & Smithsonian, Observatory Building E, 60 Garden St, Cambridge, MA 02138, USA*
[14]*Center for Space and Habitability, University of Bern, Gesellschaftsstrasse 6, CH-3012 Bern, Switzerland*
[15]*Physikalisches Institut, University of Bern, Sidlerstrasse 5, CH-3012 Bern, Switzerland*
[16]*Department of Astrophysics, University of Oxford, Denys Wilkinson Building, Keble Road, Oxford OX1 3RH, UK*
[17]*Magdalen College, University of Oxford, Oxford OX1 4AU, UK*
[18]*LESIA, Observatoire de Paris, CNRS, Université Paris Diderot, Université Pierre et Marie Curie, Meudon, France*
[19]*Université Paris-Saclay, Université Paris Cité, CEA, CNRS, AIM, F-91191, Gif-sur-Yvette, France*
[20]*Komaba Institute for Science, The University of Tokyo, 3-8-1 Komaba, Meguro, Tokyo 153-8902, Japan*
[21]*Oukaimeden Observatory, High Energy Physics and Astrophysics Laboratory, Cadi Ayyad University, Marrakech, Morocco*
[22]*Universidad Nacional Autónoma de México, Instituto de Astronomía, AP 70-264, Ciudad de México 04510, México*
[23]*Space Sciences, Technologies and Astrophysics Research (STAR) Institute, Université de Liége, Allée du 6 Août 19C, B-4000 Liége, Belgium*
[24]*Astrobiology Center, 2-21-1 Osawa, Mitaka, Tokyo 181-8588, Japan*
[25]*Cavendish Laboratory, JJ Thomson Avenue, Cambridge CB3 0HE, UK*
[26]*Institute for Particle Physics and Astrophysics, ETH Zürich, Wolfgang-Pauli-Strasse 2, CH-8093 Zürich, Switzeland*
[27]*Kotizarovci Observatory, Sarsoni 90, 51216 Viskovo, Croatia*
[28]*Faculty of Science, Astronomy and Space Sciences Department, Ankara University, Tandogan TR-06100, Türkiye*
[29]*Astronomy and Space Sciences Research and Application Center (Kreiken Observatory), Ankara University, Incek Blvd., TR-06837 Ahlatlıbel, Ankara, Türkiye*
[30]*Department of Physics and Astronomy, Georgia State University, Atlanta, GA 30303, USA*

This paper has been typeset from a TEX/LATEX file prepared by the author.